Research Square

Preprints are preliminary reports that have not undergone peer review.
They should not be considered conclusive, used to inform clinical practice,
or referenced by the media as validated information.

Spatially guided development of a hypoxia-inducible factor 1α-binding ligand for penumbra identification and targeted nanotherapy in ischaemic stroke

Yusheng Zhang
China Academy of Chinese Medical Sciences
Hong Wang
China Academy of Chinese Medical Sciences
Yiwan Geng
Chinese Academy of Sciences
Qing Wang
Beijing University of Chinese Medicine
Zhiguo Lu
Chinese Academy of Sciences
Shaoqi Song
Shanxi University of Traditional Chinese Medicine
Jie Wang
China Academy of Chinese Medical Sciences
Xin Zhang
Chinese Academy of Sciences
Hongjun Yang
China Academy of Chinese Medical Sciences
Xianyu Li
phd_xianyuli@foxmail.com

China Academy of Chinese Medical Sciences

Research Article

Keywords: stroke, ischaemic penumbra, hypoxia-inducible factor 1α, Fab' fragment, targeted drug delivery

Posted Date: November 26th, 2026

DOI: https://doi.org/10.21203/rs.3.rs-11676875/v1

License: This work is licensed under a Creative Commons Attribution 4.0 International License.
Read Full License

Additional Declarations: No competing interests reported.

Spatially guided development of a hypoxia-inducible factor 1α-binding ligand for penumbra identification and targeted nanotherapy in ischaemic stroke

Yusheng Zhang[1,#], Hong Wang[1,#], Yiwan Geng[5,#], Qing Wang[3,#], Zhiguo Lu[5], Shaoqi Song[2], Jie Wang[1], Xin Zhang[5,*], Hongjun Yang[1,4,*], Xianyu Li[1,4,*]

[1] Experimental Research Center, China Academy of Chinese Medical Sciences, Beijing 100700, China

[2] College of Basic Medicine, Shanxi University of Chinese Medicine, Taiyuan 030619, China

[3] School of Life Sciences, Beijing University of Chinese Medicine, Beijing, 100700, China

[4] State Key Laboratory for Quality Ensurance and Sustainable Use of Dao-di Herbs, China Academy of Chinese Medical Sciences, Beijing 100029, China

[5] State Key Laboratory of Biopharmaceutical Preparation and Delivery, Institute of Process Engineering, Chinese Academy of Sciences, Beijing 100190, China

# These authors contributed equally.

* Correspondence: Xianyu Li (phd_xianyuli@foxmail.com), Hongjun Yang (hongjun0420@vip.sina.com), Xin Zhang (xzhang@ipe.ac.cn)

Abstract

Background: The ischaemic penumbra contains salvageable tissue and is a principal target for stroke therapy. However, identifying molecular ligands that direct carriers to this region remains challenging. We developed a penumbra-directed delivery strategy guided by spatial transcriptomics and ischaemic tissue biology.

Results: Hypoxia-inducible factor 1α (HIF-1α) was prioritised as a candidate target, and a Fab′ fragment derived from the monoclonal antibody 41D9F1 retained antigen binding after conjugation to T7-functionalised poly(ethylene glycol)–poly(lactic-co-glycolic acid) (PEG–PLGA) nanoparticles. Treatment with intact 41D9F1 increased HIF-1α abundance in ischaemic brain tissue. The dual-functionalised nanoparticles enhanced brain drug accumulation and exhibited peri-infarct fluorescence enrichment. Combined with histology, this signal guided regional sampling and proteomics, revealing

distinct molecular profiles across putative penumbra, infarct and non-infarct regions. In rats with permanent middle cerebral artery occlusion, the formulation loaded with tanshinone IIA and hydroxysafflor yellow A yielded a mean oedema-corrected infarct volume of 12.50%, compared with 40.45% in saline-treated model animals, and improved cerebral perfusion.

Conclusions: These findings support applications in regional tissue research and therapeutic delivery.

Keywords: stroke, ischaemic penumbra, hypoxia-inducible factor 1α, Fab′ fragment, targeted drug delivery

Background

Following arterial occlusion, tissue surrounding the infarct core may retain cellular viability despite functional impairment, forming the ischaemic penumbra [1]. Its potential for recovery, together with the risk of progression to irreversible injury, makes its identification and preservation central to stroke research and treatment [2–5]. In experimental studies, locating this region allows investigation of molecular changes associated with tissue survival and responses to intervention. For therapy, drug accumulation in the brain or ischaemic hemisphere does not necessarily indicate adequate delivery to salvageable tissue [6,7]. A strategy that recognises and accesses the penumbra could thus help delineate tissue for biological investigation while directing therapeutic carriers towards tissue that may still benefit from treatment.

Ligand-mediated recognition offers one approach to directing imaging probes and therapeutic carriers towards the penumbra. The challenge is to distinguish a region defined by local ischaemic severity and tissue viability within the surrounding brain tissue. Ligand development therefore requires candidate targets whose spatial distribution reflects the tissue state of interest and distinguishes it from adjacent regions [8,9]. However, molecules induced during ischaemia may also contribute to hypoxic adaptation, metabolic regulation and tissue repair [10–12]. Engaging these molecules could alter the processes that support tissue survival. Ligand design should therefore consider both regional recognition and the consequences of binding, aiming to avoid compromising beneficial endogenous functions [13].

Spatial transcriptomics measures gene expression within its tissue context, enabling comparison of molecular programmes across neighbouring regions and identification of candidates associated with local tissue states [14]. Their roles in ischaemic stress, adaptation and repair can then inform prioritisation, bringing regional distribution together with biological relevance [15–17]. Examination of protein localisation can assess whether the corresponding protein shows a regional distribution consistent with the transcriptomic pattern. Antibodies can be screened for recognition of selected regions of a candidate protein, with the consequences of binding assessed alongside antigen specificity. The antigen-binding fragment of a selected antibody can subsequently be displayed on a carrier surface to provide recognition for fluorescent tracing or therapeutic delivery [18–20].

Here, we used a spatially guided and biology-informed strategy to develop a ligand for penumbra identification and targeted therapy. Spatial transcriptomic screening was followed by temporal, cross-model and protein-level spatial evaluation to prioritise HIF-1α. We generated the monoclonal antibody 41D9F1 against its oxygen-dependent degradation domain, assessed antigen recognition and effects on HIF-1α abundance, and displayed the derived Fab′ on T7-functionalised PEG-PLGA nanoparticles. Fluorescently labelled carriers were evaluated for penumbra identification by combining fluorescence imaging with histology, followed by regional sampling and proteomic analysis. Nanoparticles coloaded with tanshinone IIA and hydroxysafflor yellow A were separately assessed for brain drug accumulation and acute effects on infarct volume and cerebral perfusion (Fig. 1A).

Methods

Experimental animals and ethics

Female BALB/c mice aged 6-8 weeks (18-22 g) were used for monoclonal antibody production. Male Sprague-Dawley rats aged 8-10 weeks (250-300 g) were used for the cerebral ischemia experiments and were obtained from the Department of Laboratory Animal Science, Peking University Health Science Center. All animals were housed under controlled conditions at 23 ± 1 °C and 50%-85% relative humidity, with free access to food and water. All animal procedures were approved by the Experimental

Animal Ethics Committee of the Experimental Research Center, China Academy of Chinese Medical Sciences (approval no. ERCCACMS21-2402-02).

Integration of spatial transcriptomic datasets

We integrated spatial transcriptomic datasets from an endothelin-1 (ET-1)-induced cerebral ischemia model (NCBI BioProject PRJNA952594) [21], a photothrombotic stroke model available through StrokeMap [22], and an MCAO-reperfusion model available through the DREAM database [23]. The ET-1 data were aligned to the mouse GRCm38/mm10 reference genome using Space Ranger 1.0.0 and initially processed with STUtility 0.1.0. Tissue-covered spots with at least 100 total unique molecular identifiers (UMIs) were retained, and genes with fewer than 100 total UMIs across the dataset or detected in fewer than five spots were excluded. Four representative ET-1 sections, corresponding to sham, day 2, day 10 and day 21, were included. Expression values were log-normalized to 10,000 counts per spot for spatial visualization, regional summaries and gene-effect estimation. The acute day-2 section was used for candidate discovery. To avoid circular inference, lesion regions were defined without using *Hif1a* expression or the HIF-1 response score. The day-2 section was processed using SCTransform with regularized negative-binomial regression, followed by principal-component analysis and nearest-neighbour graph construction using the first 30 principal components. Graph-based clustering was performed at a resolution of 2 with a fixed random seed of 2026. For each cluster, an acute-injury score was calculated from *Lgals3, Cd68, Ctsb, Ctsd, Cst7, Tyrobp, Lyz2, Spp1, Apoe, C1qa, C1qb* and *C1qc*, and transcript complexity was represented by the median number of detected genes per spot. The core-like cluster was selected from clusters in the upper quartile of the acute-injury score and the lower quartile of transcript complexity, with the lowest-complexity eligible cluster retained [21,24,25].

An exact six-neighbour graph was then constructed from the Visium hexagonal coordinates. The cluster sharing the largest direct boundary with the core-like cluster was designated the inner peri-lesional region, whereas the cluster sharing the largest boundary with the inner region, after excluding the core-like and inner clusters, was designated the outer peri-lesional region. All remaining spots were classified as distal tissue. The inner and outer peri-lesional regions were combined to form an operational putative-penumbra compartment.

For candidate screening, raw counts were aggregated separately across the putative-penumbra and distal compartments, converted to counts per million and expressed as $\log_2$[(CPM_putative penumbra + 0.5)/(CPM_distal + 0.5)]. Genes with fewer than 20 combined counts were removed, and the remaining genes were ranked by their putative-penumbra-versus-distal effects. Unbiased preranked gene-set enrichment analysis was performed using fgseaMultilevel against all Gene Ontology Biological Process terms mapped with org.Mm.eg.db and GO.db. Gene sets containing 10-500 detected genes were retained, and false-discovery rates were controlled using the Benjamini-Hochberg procedure.

The within-programme rank of *Hif1a* was determined by ordering genes within each hypoxia-, metabolic- or angiogenesis-associated gene set according to their putative-penumbra-versus-distal effect. A predefined HIF-1 response score was independently calculated from 25 canonical downstream genes [26,27]: *Slc2a1, Hk2, Gpi1, Pfkl, Aldoa, Tpi1, Gapdh, Pgk1, Eno1, Pkm, Ldha, Pdk1, Vegfa, Bnip3, Bnip3l, Ndrg1, Ddit4, Egln3, P4ha1, P4ha2, Plod1, Adm, Mif, Pgf* and *Angptl4*. The expression of each gene was *z*-standardized across all spatial spots and then averaged, with *Hif1a* explicitly excluded from the score. Regional distributions of *Hif1a* expression and the HIF-1 response score were compared using two-sided Wilcoxon rank-sum tests. The same day-2 regional annotation was used for segmentation and both regional comparisons. For *Hif1a*, the outer peri-lesional and distal regions were combined for the three-compartment display. *p* values were adjusted using the Benjamini–Hochberg procedure across the three comparisons in each panel. Spot-level comparisons were interpreted as spatial summaries rather than animal-level inference, because spots do not constitute independent biological replicates [28]. For temporal analysis, spatial *Hif1a* expression was examined in the sham, day-2, day-10 and day-21 ET-1 datasets. Regionally differential genes at each time point were identified using the Wilcoxon rank-sum test, with a minimum detection rate of 10%, an absolute average $\log_2$ fold change greater than 1 and a Bonferroni-adjusted *p* value below 0.05. The resulting gene lists were subjected to mouse KEGG over-representation analysis, and pathways passing the predefined *q*-value threshold were summarized together with the subset containing *Hif1a*. For the photothrombotic and MCAO-reperfusion models, spatial expression patterns were examined directly using the web-based analysis portals linked to the original publications, namely StrokeMap and the DREAM database. Portal-provided histological images,

regional annotations and spatial expression maps were used to identify the infarct core, proximal and distal peri-infarct regions, non-infarct tissue and the ipsilateral and contralateral hemispheres. Spatial distributions of *Hif1a* and the representative downstream target *Vegfa* were then evaluated across these predefined anatomical regions. Because complete raw spot-level data were not uniformly accessible through the two external portals, these datasets were used for qualitative cross-model validation of *Hif1a* localization rather than for pooled statistical inference.

HIF-1α immunogen, candidate peptides, and animal immunization

A His-tagged recombinant rat HIF-1α fragment (Rat HIF-1α-His, residues 380-585; UniProtKB O35800) was produced in suspension-adapted HEK293F/Expi293 cells (CUSABIO Technology LLC, Wuhan, China) and used as the immunogen. The fragment encompasses the principal region of the HIF-1α oxygen-dependent degradation domain (ODD). After Ni-NTA affinity purification, purity and integrity were assessed by SDS-PAGE, and the concentration was determined with a bicinchoninic acid (BCA) assay. Aliquots were stored at -80 °C and were not subjected to repeated freeze-thaw cycles. Two site-directed screening peptides spanning the region adjacent to HIF-1α Pro564 were designed: BSA-Cys-QDTDLDLEMLAPYIPMDD and DLEMLAPYIPMDDDFQLR-Cys-BSA. The peptides were prepared by solid-phase synthesis, purified by high-performance liquid chromatography (HPLC), and coupled to BSA through the terminal cysteine for site-focused secondary screening of hybridomas. Female BALB/c mice aged 6-8 weeks (18-22 g) were immunized. For the primary immunization, each mouse received 50 μg Rat HIF-1α-His at multiple subcutaneous sites after emulsification with an equal volume of complete Freund's adjuvant. Three booster immunizations with the same antigen dose in incomplete Freund's adjuvant were administered at 2-week intervals. Peripheral blood was collected after boosting, and serum antibody titers were measured by indirect ELISA using Rat HIF-1α-His (residues 380-585) as the coating antigen. An endpoint titer of at least 1:64,000 was used as a reference criterion for cell fusion. Three days before fusion, each mouse received a 50 μg booster of recombinant immunogen without adjuvant. Mice with high serum titers, strong antigen reactivity, and good overall condition were selected for hybridoma generation.

Hybridoma screening and identification of 41D9F1

Three days after the final booster, mice were euthanized according to the approved animal protocol. Spleens were aseptically collected and processed into splenocyte suspensions. Splenocytes were mixed with logarithmically growing SP2/0 mouse myeloma cells (CUSABIO Technology LLC, Wuhan, China) and fused with PEG 1450/1500 cell-fusion reagent. The fused cells were seeded into 96-well plates and selected in HAT medium. Once hybridoma colonies formed, cultures were progressively transferred to HT medium and then to conventional complete medium according to growth status.

Hybridoma supernatants were first screened by indirect ELISA using the recombinant Rat HIF-1α-His fragment (residues 380-585) as the coating antigen. Positive clones were then rescreened by ELISA against the two Pro564-adjacent peptide-BSA conjugates, with BSA alone serving as a control to exclude anti-BSA antibodies and nonspecific binding. ELISA-positive hybridomas underwent multiple rounds of limiting-dilution subcloning, and culture supernatants were retested until stable antibody secretion from monoclonal cell lines was established.

Candidate antibodies were further validated in U87 and HeLa cells (CUSABIO Technology LLC, Wuhan, China). Fixed and permeabilized cells were sequentially incubated with candidate antibodies and fluorescent secondary antibodies. The proportion of positive cells and mean fluorescence intensity were measured by flow cytometry (BD Biosciences, USA) to assess recognition of endogenous intracellular HIF-1α. Samples without primary antibody and samples incubated with an isotype-matched antibody were included to define background signals. In parallel, western blotting was used to determine whether candidate antibodies recognized the HIF-1α immunoreactive band. Samples included HeLa, HepG2, U87, SH-SY5Y, JK-1, MCF-7, and CP-R137 cells (CUSABIO Technology LLC, Wuhan, China), together with mouse and rat skeletal muscle. HIF-1α bands at approximately 110-130 kDa were examined.

Lead clones were selected by integrating ELISA binding to the recombinant immunogen, reactivity with Pro564-adjacent peptides, intracellular flow-cytometry results, and western blot band recognition. Total RNA was isolated from positive hybridomas, reverse transcribed, and used to amplify and sequence the variable regions of the antibody heavy and light chains (VH and VL). Eukaryotic expression vectors

encoding the heavy and light chains were constructed from these sequences and cotransfected into HEK293F/Expi293 cells for transient expression. Recombinant antibodies were purified from culture supernatants by Protein A affinity chromatography and quantified by BCA assay. Antigen-binding activity and recognition characteristics were confirmed by ELISA, intracellular flow cytometry, and western blotting, leading to the final selection of the HIF-1α monoclonal antibody 41D9F1.

Ex vivo brain fluorescence imaging and assessment of intracerebral distribution

To evaluate the distribution and retention of 41D9F1 in infarct-associated brain regions, FITC-labeled 41D9F1 (FITC-41D9F1) was used for intracerebral tracing, with free FITC as the control at a matched fluorophore dose and injection volume. Sprague-Dawley rats were anesthetized with inhaled isoflurane and secured in a stereotaxic frame with bregma and lambda at the same level. Using bregma as the origin, FITC-41D9F1 was injected into the left peri-infarct cortex at AP +1.0 mm, ML -2.0 mm, and DV -1.2 mm; sham-operated rats were injected at the corresponding site in the left cortex. A Hamilton microsyringe was used to deliver 2 μL FITC-41D9F1 (2.5 μg/μL; total dose, 5 μg) at 0.2 μL/min. The needle was left in place for 1 min before slow withdrawal and wound closure. DiR-labeled nanoparticles were used separately to assess how surface functionalization affected brain distribution. At 2 h after permanent MCAO (p-MCAO), rats received DiR-labeled PS, T7-PS, or T7/HIF-PS by tail-vein injection at a DiR dose of 0.5 mg/kg with matched injection volumes. Six hours after intracerebral FITC-41D9F1 injection or intravenous nanoparticle administration, rats were terminally anesthetized with sodium pentobarbital (60 mg/kg, intraperitoneally) and transcardially perfused with ice-cold PBS to remove circulating blood and unbound fluorophore. Whole brains were rapidly excised, gently blotted, and immediately imaged ex vivo with an IVIS Spectrum system (PerkinElmer, USA).

Enzyme-linked immunosorbent assay

An untreated normal group and two sham-operated groups were used for the non-ischaemic experiment. Sham-operated rats received the intact 41D9F1 monoclonal antibody (1 mg/kg) or an equal volume of PBS by tail-vein injection; normal rats underwent neither surgery nor treatment. Brains were collected 6 h after injection or at the matched time in untreated rats. HIF-1α in tissue-homogenate supernatants was measured with a rat HIF-1α ELISA kit (UpingBio, Hangzhou, China; catalog no. SYP-R0129) according

to the manufacturer's instructions. Samples were clarified by centrifugation at 4 °C, and supernatants and serial standards were added to precoated 96-well plates. After sequential incubation with the detection antibody and enzyme conjugate and the prescribed washing steps, TMB substrate was added and developed in the dark. The reaction was stopped, and absorbance was measured at 450 nm with 570 or 630 nm as the reference wavelength. HIF-1α concentrations were calculated from the standard curve and sample dilution factors. All samples were analyzed in replicate with appropriate blank controls.

SDS-PAGE analysis

PS, T7-PS and T7/HIF-PS were purified by ultrafiltration and normalized to equal particle numbers. Samples were mixed with 4× non-reducing SDS-PAGE loading buffer to a final concentration of 1×, heated at 95 °C for 10 min and resolved on a 10% polyacrylamide gel alongside a molecular-weight marker. After Coomassie Brilliant Blue staining and destaining, protein bands were compared among the three formulations. A band at approximately 50–55 kDa in T7/HIF-PS, but not in PS or T7-PS, was considered consistent with Fab′-associated protein in the nanoparticle preparation.

HIF-1α antigen magnetic-bead capture assay

To assess whether nanoparticle-conjugated Fab′ retained antigen-binding activity, a recombinant rat HIF-1α fragment was covalently immobilized on Pierce NHS-Activated Magnetic Beads (Thermo Fisher Scientific) according to the manufacturer's instructions. Briefly, 300 μL of bead suspension (10 mg/mL; 3 mg of beads) was washed with ice-cold 1 mM HCl and immediately mixed with 300 μL of antigen solution (0.5 mg/mL; 150 μg of antigen input) prepared in amine-free 50 mM borate buffer (pH 8.5). The mixture was rotated for 2 h at room temperature. After magnetic separation and washing, residual reactive groups were quenched with 3 M ethanolamine (pH 9.0) for 2 h at room temperature. For each capture reaction, 0.25 mg of antigen-coupled beads was incubated with coumarin-6-labelled PS, T7-PS or T7/HIF-PS for 1 h at room temperature in the dark. Nanoparticle inputs were matched by particle number, and input fluorescence was recorded for normalization. Beads processed identically without antigen served as background controls. Following magnetic separation, beads were washed with PBS containing 0.05% Tween-20, resuspended in PBS and transferred to a black 96-well plate. Bead-associated

fluorescence was corrected using the antigen-free bead signal and normalized to input fluorescence; group comparisons were expressed relative to the PS signal.

Synthesis and characterization of PEG-PLGA copolymers

NH_2-PEG_{5k}-OH was dissolved in anhydrous dichloromethane, and MAL-3-NHS was added at 0 °C in the presence of N,N-diisopropylethylamine under nitrogen. The mixture was then warmed to room temperature and reacted overnight. MAL-PEG_{5k}-OH was obtained by precipitation, purification, and vacuum drying. MAL-PEG_{5k}-OH or mPEG_{5k}-OH was used as a macroinitiator, with $Sn(Oct)_2$ as the catalyst, to initiate ring-opening polymerization of lactide and glycolide at a 75:25 molar ratio (Chongqing Bojingchi Pharmaceutical Technology Co., Ltd., Chongqing, China). After degassing and vacuum sealing, the reaction was conducted at 150 °C for 48 h to yield MAL-PEG_{5k}-$PLGA_{15k}$ and mPEG_{5k}-$PLGA_{15k}$. Crude products were purified by repeated precipitation and vacuum-dried to constant mass.

Preparation and surface conjugation of dual-drug nanoparticles

mPEG_{5k}-$PLGA_{15k}$ and MAL-PEG_{5k}-$PLGA_{15k}$ were mixed at an 80:20 molar ratio and dissolved with TanIIA (Chengdu Must Bio-Technology Co., Ltd., Chengdu, China) in anhydrous acetone to form the organic phase. HSYA (Chengdu Must Bio-Technology Co., Ltd., Chengdu, China) was dissolved in deionized water to form the aqueous phase. The feed mass ratios of TanIIA and HSYA to total polymer were 1:30 and 1:24, respectively. Under continuous stirring, the organic phase was added dropwise to the aqueous phase at a constant rate, producing dual-drug nanoparticles by solvent diffusion and polymer self-assembly. The dispersion was stirred for another 8 h to remove organic solvent, allowed to stand for 1 h, passed through a 0.22 μm filter, and purified at 4 °C and 4,000 × *g* with a 100 kDa centrifugal ultrafilter. After three PBS washes, TanIIA/HSYA@PS was obtained [29].

Purified 41D9F1-derived $F(ab')_2$ was supplied by CUSABIO Technology LLC (Wuhan, China). To generate Fab′ with free hinge-region thiols, $F(ab')_2$ was reduced in PBS containing 4 mmol/L EDTA using 2-mercaptoethylamine hydrochloride (2-MEA; Thermo Scientific Pierce, catalog no. 20408) at a final concentration of 50 mmol/L for 90 min at 37 °C, following the manufacturer's recommended reduction conditions. After cooling to room temperature, residual 2-MEA was promptly removed by

buffer exchange using a 50 kDa centrifugal ultrafilter before maleimide coupling. The resulting 41D9F1 Fab′ was then reacted with TanIIA/HSYA@PS for 4 h at room temperature in PBS, pH 7.4, at a theoretical feed density of approximately one Fab′ per particle. Unbound Fab′ was removed by 100 kDa ultrafiltration. The N-terminal cysteine-containing T7 peptide H-Cys-HAIYPRH-NH_2 (Tocris Bioscience, Bristol, UK) was then added at a theoretical feed density of approximately seven T7 molecules per particle and reacted for another 4 h. After removal of unconjugated T7 by ultrafiltration, residual maleimide groups were quenched with L-cysteine to yield TanIIA/HSYA@T7/HIF-PS. Ligand preparation and conjugation were performed under nitrogen and protected from light.

Particle size, ζ potential, morphology, and ligand identification

Nanoparticle dispersions were diluted to an appropriate concentration with ultrapure water, and particle-size distributions and ζ potentials were measured with a ZetaView nanoparticle tracking analysis system. Data were acquired at 11 positions in the sample cell using a 488 nm laser, a sensitivity setting of 80, and a shutter setting of 100. The particle-number-based median hydrodynamic diameter, X50, was extracted from each report; the three X50 measurements per formulation were summarized as mean ± SD. ζ potential measurements were summarized separately as mean ± SD. Nanoparticle morphology was examined by transmission electron microscopy. Appropriately diluted dispersions were deposited on carbon-coated copper grids and allowed to adsorb, after which excess liquid was removed. Samples were negatively stained with 2% uranyl acetate when required, dried at room temperature, and imaged with a transmission electron microscope (Hitachi, Ltd., Japan) at an accelerating voltage of 100 kV.

Encapsulation efficiency, drug loading, and in vitro release

After preparation and purification by 100 kDa ultrafiltration, TanIIA/HSYA@PS, TanIIA/HSYA@T7-PS, and TanIIA/HSYA@T7/HIF-PS dispersions were analyzed for drug content. Each dispersion was divided into two aliquots for separate quantification of HSYA and TanIIA using their respective external calibration curves. For HSYA analysis, the aliquot was mixed with an equal volume of methanol-water (1:1, v/v), vortexed, and sonicated to release the encapsulated drug. For TanIIA analysis, the aliquot was extracted with methanol-DMSO (9:1, v/v) and mixed thoroughly. After centrifugation, the supernatants were analyzed by HPLC (Agilent Technologies, USA).

HSYA was separated on a Sina-Chrom ODS-BP C18 column (4.6 × 250 mm, 5 μm) using methanol and 0.1% aqueous phosphoric acid (32:68, v/v) at 0.8 mL min^{-1}. Detection was performed at 410 nm with a 5 μL injection volume and an 18 min run time; the retention time was approximately 11.083 min [30]. TanIIA was separated on a ChromCore C18 column (3 × 150 mm, 3 μm) using methanol and 0.1% aqueous phosphoric acid (83:17, v/v) at 0.35 mL min^{-1}. Detection was performed at 270 nm with a 3 μL injection volume and an 18 min run time; the retention time was approximately 9.497 min [31].

The encapsulated masses of HSYA and TanIIA (W_encap,i) were calculated from their respective peak areas and calibration curves after correction for dilution and sampled volume. To determine nanoparticle dry mass (W_NP), a defined volume of each purified dispersion was buffer-exchanged into ultrapure water and lyophilized to constant weight. Encapsulation efficiency (EE) and drug loading (DL) were calculated separately for each drug as follows:

$$\mathrm{EE}\ (\%) = \frac{\mathrm{Wencap}}{\mathrm{Wfeed}} \times 100\%$$

$$\mathrm{DL}\ (\%) = \frac{\mathrm{Wencap}}{\mathrm{WNP}} \times 100\%$$

Where W_encap is the mass of the corresponding drug encapsulated in the purified nanoparticles, W_feed is the initial mass of that drug used during nanoparticle preparation, and W_NP is the total dry mass of the corresponding drug-loaded nanoparticles. Each formulation was analyzed in at least triplicate, and identically processed blank nanoparticles were used as matrix controls.

In vitro release of TanIIA and HSYA from the three formulations was assessed by dialysis, with the corresponding free drugs as controls. Formulations and free-drug controls were placed in 10 kDa dialysis bags pre-equilibrated with the corresponding buffer, and the initial mass of each drug in the bag was recorded. Each bag was immersed in 30 mL of release medium and gently agitated at 100 rpm and 37 °C. Release was assessed in pH 7.4 PBS and an acidic, lipase-containing system at pH 5.0. For the latter condition, lipase was added to the sample inside the bag before sealing to a final activity of 1,000 U/mL, and both the internal and external media were adjusted to pH 5.0. At prespecified times over 36 h, equal-volume aliquots of the external medium were withdrawn and immediately replaced with the same volume of fresh corresponding medium prewarmed to 37 °C. TanIIA and HSYA were quantified separately by

HPLC under the conditions described above. Cumulative release included the drug remaining in the external medium and the amount removed in all previous aliquots and was expressed as a percentage of the initial mass of the corresponding drug in the bag. Three parallel dialysis units were used for each formulation under each release condition.

Permanent middle cerebral artery occlusion model, experimental groups, and treatment

Permanent occlusion of the left middle cerebral artery (p-MCAO) was induced with a modified intraluminal filament technique. Adult male Sprague-Dawley rats (250-300 g) were acclimatized for 5 d and fasted for 12 h before surgery with water available ad libitum. Rats were anesthetized with sodium pentobarbital (60 mg/kg, intraperitoneally), and body temperature was maintained throughout surgery. The left common carotid artery (CCA), external carotid artery (ECA), and internal carotid artery (ICA) were isolated while preserving the vagus nerve. The CCA and ICA were temporarily clamped, the distal ECA was ligated, and a silicone-coated nylon filament matched to body weight was inserted through a proximal ECA incision. The filament was advanced approximately 18-20 mm along the ICA until slight resistance was felt and was secured to occlude the origin of the middle cerebral artery. The filament remained in place permanently, without reperfusion. Sham-operated rats underwent vessel exposure without filament insertion. Animals exhibiting neurological deficits such as contralateral forelimb flexion, ipsiversive walking, or spontaneous circling were included in the study.

Rats were randomly assigned to seven groups: sham control (Control), saline-treated p-MCAO (Model), blank carrier (PS), dual-functionalized blank carrier (T7/HIF-PS), TanIIA monotherapy (TanIIA@T7/HIF-PS), HSYA monotherapy (HSYA@T7/HIF-PS), and dual-drug treatment (TanIIA/HSYA@T7/HIF-PS). All groups except the Control group underwent p-MCAO.

Treatments were administered by tail-vein injection 2 h after p-MCAO. The Control and Model groups received equal volumes of saline. The dual-drug formulation delivered TanIIA and HSYA at 10 and 4 mg/kg, respectively. The corresponding monotherapy groups received TanIIA at 10 mg/kg or HSYA at 4 mg/kg. T7/HIF-PS and PS were administered at the same particle number as the dual-drug formulation. Injection volumes were matched across groups. Neurological function and survival were monitored, and tissues were collected 6 h after treatment.

Quantification of drugs in brain tissue

To evaluate brain delivery of the dual-drug nanomedicine, TanIIA/HSYA@PS, TanIIA/HSYA@T7-PS and TanIIA/HSYA@T7/HIF-PS were administered by tail-vein injection 2 h after p-MCAO, each at a TanIIA dose of 10 mg/kg and with matched injection volumes. Six hours after administration, deeply anesthetized rats were cannulated through the left ventricle, the right atrial appendage was incised, and animals were perfused with ice-cold saline until the effluent was clear to remove residual blood and circulating free drug. Whole brains were rapidly excised, blotted, and weighed. Brain tissue was homogenized on ice in ice-cold saline or PBS at a tissue-to-liquid ratio of 1:4 and divided into two aliquots for HSYA and TanIIA quantification. Three volumes of methanol were added to HSYA samples, which were vortexed for 3 min and incubated on ice for 10 min. Four volumes of methanol-DMSO (9:1, v/v) were added to TanIIA samples, followed by vortexing and sonication for 10 min to release drug from the tissue matrix and nanoparticles. Samples were centrifuged at 12,000 rpm for 10 min at 4 °C, and the supernatants were filtered through 0.22 μm membranes before HPLC analysis (Agilent Technologies, USA).

Cellular uptake and fluorescence imaging

RBE4 brain microvascular endothelial cells and SH-SY5Y neuron-like cells were cultured at 37 °C in 5% CO_2. For hypoxic experiments, cells were preconditioned at 1% O_2 for 2 h and subsequently incubated under the same hypoxic conditions for 6 h with coumarin-6-labelled PS, T7-PS, or T7/HIF-PS at a coumarin-6-equivalent concentration of 50 ng/mL. Normoxic cultures were treated in parallel. For HIF-1α inhibition experiments, CAY10585 was used at a final concentration of 20 μM. After three washes with PBS, cells were harvested by trypsinisation, and mean fluorescence intensity was measured by flow cytometry. Three independent experiments were performed per group. For fluorescence imaging, cells were fixed with 4% paraformaldehyde, counterstained with DAPI, and imaged using identical exposure settings, with consistent thresholds applied during image analysis.

TTC staining and oedema-corrected infarct volume

Brains were collected 6 h after treatment and cut coronally into 2 mm slices. Sections were incubated in 2% 2,3,5-triphenyltetrazolium chloride (TTC) for 20 min at 37 °C in the dark. Fiji/ImageJ was used to

delineate the contralateral hemisphere and non-infarcted ipsilateral tissue on digitized slices, excluding the surrounding background. Areas were summed across equal-thickness slices. Oedema-corrected infarct volume was calculated as follows: [contralateral hemispheric area - non-infarcted area of the ipsilateral hemisphere]/contralateral hemispheric area × 100%.

Laser speckle imaging of cerebral blood flow

Cerebral perfusion in ischemic regions was assessed with a moorFLPI-2 laser speckle contrast imaging system (Moor Instruments Ltd., UK). At prespecified time points, rats were anesthetized by intraperitoneal sodium pentobarbital and secured on a temperature-controlled surgical platform. Body temperature was maintained at 37.0 ± 0.5 °C. A midline scalp incision was made, connective tissue was gently removed from the skull, and the calvarium was kept intact while bleeding was avoided. The skull surface was moistened with saline during imaging. Cerebral perfusion maps were acquired at a fixed working distance using identical exposure and acquisition settings and processed with moorFLPI-2 software (version 3.0.1.000). The middle cerebral artery territory in the ischaemic hemisphere was defined as the region of interest. Mean perfusion over a stable acquisition interval was obtained directly from the software and expressed in perfusion units (PU), without division by contralateral perfusion.

Laser microdissection and regional quantitative proteomics

At 2 h after p-MCAO, rats received T7/HIF-PS nanoparticles loaded with DiI by tail-vein injection. Brains were collected by transcardial perfusion 6 h after administration. Tissue was rapidly frozen in liquid nitrogen and cut into serial 10 μm cryosections mounted on either MMI PET membrane slides for laser microdissection or conventional glass slides for rapid hematoxylin and eosin staining and histological orientation. All fluorescence sections were imaged as whole slides using identical exposure times, gain, and excitation and emission settings. Adjacent hematoxylin and eosin and fluorescence sections were affinely registered using stable anatomical landmarks, including the outer brain contour, lateral ventricle, and corpus callosum.

All sampling regions were restricted to the ipsilateral cerebral cortex. DiI images were segmented semiautomatically using StrataQuest 7.1 (TissueGnostics). Fluorescence thresholds were set manually with reference to morphologically preserved cortical areas with low DiI fluorescence. Initial software-

generated masks were overlaid on the original images and refined using adjacent H&E sections and anatomical landmarks, excluding folds, section-edge artifacts and isolated non-target signals. The infarct region (IR) was delineated by disrupted architecture, reduced cellular density or attenuated H&E staining. Peri-infarct cortex with increased DiI fluorescence and comparatively preserved architecture was operationally defined as the putative penumbra zone (PZ). Low-fluorescence, morphologically preserved ipsilateral cortex outside these regions was designated the non-infarct region (NIR). Binary BigTIFF masks were imported into MMI CellTools 6.0 and aligned using anatomical landmarks; alignment was checked against live microscope images and adjusted where necessary. Target regions were isolated using an MMI CellCut system and MMI Isolation Caps (Molecular Machines & Industries, Switzerland). Equal cumulative tissue areas were collected from each region of each animal and pooled into one sample per region per animal, preserving animal identifiers. Samples were processed using a SISPROT FLEX low-input proteomics sample-preparation kit (BayOmics, BO-012-24, China) for lysis, enrichment, reduction, alkylation, tryptic digestion and desalting. Regional differential abundance was evaluated with limma using region as the group factor; animal identity was not included as a blocking factor in this model. Proteins with $p < 0.05$ and $|\log_2 \text{fold change}| > 0.585$ in at least one regional contrast were selected for clustering. Regional mean abundances were standardized by protein and grouped by k-means into five clusters. Selected-protein comparisons in Fig. S6 retain p values from the regional limma contrasts.

Quantitative proteomics and bioinformatic analysis

An appropriate amount of infarct-hemisphere tissue was lysed in buffer containing protease and phosphatase inhibitors, homogenized on ice, sonicated, and centrifuged at low temperature. Supernatants were collected, protein concentrations were measured by BCA assay, and equal protein amounts were reduced, alkylated, and digested with trypsin. Peptides were desalted on C18 material and reconstituted in 0.1% aqueous formic acid for liquid chromatography-tandem mass spectrometry (LC-MS/MS).

Peptides were separated by nanoscale reversed-phase liquid chromatography on a C18 column. Mobile phase A was 0.1% formic acid in water and mobile phase B was 0.1% formic acid in acetonitrile. Peptides were eluted over an approximately 90 min gradient at approximately 300 nL/min. Data-independent acquisition was performed in positive-ion mode on an Orbitrap Astral LC-MS/MS system (Thermo

Fisher Scientific, USA). MS1 spectra were acquired over m/z 350-1,500 at a resolution of 120,000; automatic gain control and maximum ion-injection time were optimized for the experiment. MS2 spectra were acquired in predefined segmented isolation windows using higher-energy collisional dissociation at a normalized collision energy of 25%-30%. Quality-control samples were interspersed throughout the acquisition sequence to monitor instrument stability.

Raw data were searched and quantified with DIA-NN 1.8.1 against the UniProt rat reference proteome. Enzyme specificity was set to Trypsin/P with up to one missed cleavage. Cysteine alkylation was specified as a fixed modification, and protein N-terminal acetylation and methionine oxidation were specified as variable modifications. False discovery rates were controlled below 1% at both the peptide and protein levels. For the treatment-group comparisons, differential abundance was analysed with limma in R 4.3.3 after missing-value filtering, median normalization and $\log_2$ transformation. *p* values were adjusted using the Benjamini–Hochberg procedure. Proteins with an adjusted *p* value below 0.05 and an absolute $\log_2$ fold change greater than 1 were considered differentially abundant and were subjected to clustering, functional enrichment and coexpression-network analysis. Coexpression modules were identified with WGCNA using a soft-thresholding power of 30, an unsigned topological overlap matrix, a minimum module size of 20, deepSplit = 2 and mergeCutHeight = 0.25. Module eigengenes were correlated with binary indicators of experimental groups using Pearson correlations; *p* values were calculated with corPvalueStudent. Gene identifiers were mapped with org.Rn.eg.db. Gene Ontology and rat KEGG over-representation analyses were performed with clusterProfiler using hypergeometric tests and Benjamini–Hochberg adjustment.

Western blot validation

For the intact-antibody experiment, rats received the 41D9F1 monoclonal antibody (1 mg/kg) or an equal volume of PBS by tail-vein injection 2 h after p-MCAO, and brains were collected 6 h later. A separate cohort, selected for validation of proteomic findings, comprised Control, Model, TanIIA/HSYA@T7-PS and TanIIA/HSYA@T7/HIF-PS groups. These animals received treatment by tail-vein injection 2 h after p-MCAO, with brain collection 6 h later; Control animals underwent sham surgery. The dual-drug formulations were administered at TanIIA and HSYA doses of 10 and 4 mg/kg, respectively, and Control

and Model animals received matched vehicle volumes. Brain tissue was homogenized in ice-cold RIPA buffer containing protease and phosphatase inhibitors, lysed on ice for 30 min, and centrifuged at 12,000 rpm for 15 min at 4 °C. Supernatants were collected, protein concentrations were determined by BCA assay, and equal protein amounts were separated by 10% SDS-PAGE. Proteins were transferred to 0.45 μm PVDF membranes by wet transfer at a constant current of 300 mA for 90 min. Membranes were blocked for 1 h at room temperature in 5% BSA in TBST and incubated overnight at 4 °C with antibodies against HIF-1α (Abcam, ab179483, 1:1,000), phospho-mTOR Ser2448 (Proteintech, 80596-1-RR, 1:10,000), mTOR (Proteintech, 66888-1-Ig, 1:10,000), VEGFA (Proteintech, 26157-1-AP, 1:2,000), or β-actin (Proteintech, 66009-1-Ig, 1:1,000). Membranes were washed three times for 10 min in TBST and incubated for 1 h at room temperature with the corresponding horseradish peroxidase-conjugated goat anti-rabbit or goat anti-mouse IgG secondary antibody (Jackson ImmunoResearch, 111-035-003 or 115-035-003, 1:10,000). After further washing, signals were developed by enhanced chemiluminescence and imaged. HIF-1α, VEGFA, and mTOR abundance was normalized to β-actin, and mTOR phosphorylation was expressed as the phospho-mTOR Ser2448/mTOR densitometric ratio. Bands were quantified with ImageJ (National Institutes of Health, USA).

Brain tissue immunofluorescence and image quantification

Rat brains were collected 8 h after p-MCAO, fixed, embedded in paraffin and cut into coronal sections. Adjacent sections were stained with H&E for anatomical orientation. After deparaffinization and rehydration through graded ethanol, fluorescence sections underwent heat-induced antigen retrieval in citrate buffer (pH 6.0), followed by cooling and blocking of nonspecific binding. Sections were incubated overnight at 4 °C with rabbit anti-HIF-1α (Abcam, ab179483, 1:100) and chicken anti-GFAP (Abcam, ab4674, 1:1,000). After washing, sections were incubated for 1 h at room temperature in the dark with cross-adsorbed Alexa Fluor 488-conjugated anti-rabbit IgG (Abcam, ab150081, 1:1,000) and Alexa Fluor 594-conjugated anti-chicken IgY (Abcam, ab150176, 1:1,000), followed by DAPI nuclear counterstaining. Controls omitting primary antibodies were included. Images at matched anatomical levels were acquired using a fluorescence microscope equipped with a Nikon DS-U3 digital imaging controller (Nikon, Japan), with identical acquisition settings across samples. Co-registered image exports

were analyzed in Fiji/ImageJ. The DAPI blue channel was smoothed with a Gaussian filter (σ = 12 pixels), segmented using Otsu automatic thresholding and subjected to three binary closing operations; connected components smaller than 50,000 pixels were excluded from the tissue mask. The HIF-1α green and GFAP red channels were separately background-corrected using a rolling-ball radius of 50 pixels and segmented with the Triangle automatic threshold method. Marker-positive area was calculated as the number of positive pixels within the tissue mask divided by the total tissue-mask pixel count, multiplied by 100%. When multiple anatomically matched sections were analyzed from one animal, section-level values were averaged before animal-level analysis. Marker-specific positive areas describe thresholded spatial coverage and were not interpreted as directly comparable fluorescence intensities across antibodies.

Statistical analysis

Data are presented as mean ± standard deviation unless otherwise indicated in the figure legends. Two groups were compared with two-sided *t* tests, and multiple groups were compared by one-way analysis of variance followed by Tukey's post hoc test. Corresponding nonparametric tests were used when assumptions of normality or homoscedasticity were not met. Spatial spot-level comparisons used two-sided Wilcoxon rank-sum tests, with the correction scope specified in the spatial analysis methods and Fig. 1 legend. Animal-level and spot-level analyses were not treated as equivalent replication. Analyses were performed in SPSS 22.0 and GraphPad Prism 9.4.0. Two-sided *p* values below 0.05 were considered statistically significant.

During the preparation of this manuscript, the authors used ChatGPT (OpenAI) to assist with language editing, organisation, reference formatting and preparation of explanatory schematic elements. The authors reviewed and edited the outputs and take full responsibility for the content of the publication.

Results

Spatially guided, mechanism-informed analysis prioritizes HIF-1α as a candidate target in the ischemic penumbra

We established a spatially guided and biology-informed strategy to identify molecular candidates for ligand development in the ischaemic penumbra (Fig. 1B). The workflow combined spatial compartment definition, programme-level analysis, candidate prioritization and spatial validation. Candidate genes were evaluated according to their regional distribution, their positions within peri-lesional biological programmes and their biological relevance to hypoxic tissue. The detailed computational workflow is shown in Fig. S1F.

The acute day-2 ET-1 section was used for candidate discovery. Quality-control analysis showed comparable tissue coverage and library complexity across the ET-1 spatial transcriptomic sections (Additional file 1: Fig. S1A). Spatial clustering, an acute-injury signature, transcript complexity and Visium-grid topology delineated a core-like region, inner and outer peri-lesional layers, and distal tissue in the day-2 section (Fig. 1C). The inner and outer peri-lesional layers were combined as the putative-penumbra compartment for candidate screening.

We ranked 14,978 adequately detected genes according to their regional effects between the putative penumbra and distal tissue and performed preranked enrichment analysis across 5,833 Gene Ontology biological processes. Programmes related to hypoxia, oxygen availability and vascular adaptation were enriched in the putative penumbra (Fig. 1D). The response-to-hypoxia programme had a normalized enrichment score (NES) of 1.36 and a false-discovery rate (FDR) of 0.038, and the response to decreased oxygen levels had an NES of 1.37 and an FDR of 0.049. Angiogenesis showed stronger enrichment, with an NES of 2.12 and an FDR of 1.52×10^{-15}. The running enrichment profile for the response-to-hypoxia programme further placed *Hif1a* within the positively enriched gene set (Fig. S1G).

Candidate genes were then evaluated within the enriched programmes. *Hif1a* showed a positive regional effect in the putative penumbra and ranked highly within several programmes related to hypoxia,

metabolic adaptation and angiogenesis (Fig. 1E). Together with the established role of HIF-1α in oxygen sensing and hypoxic adaptation, these results prioritized *Hif1a* for further spatial analysis.

Spatial mapping showed focal *Hif1a* enrichment around the acute lesion (Fig. 1F). Mean log-normalized expression was highest in the inner peri-lesional layer (0.72), compared with the core-like region (0.40), outer peri-lesional layer (0.34) and distal tissue (0.36). Expression was higher in the inner peri-lesional layer than in the core-like region (adjusted $p = 0.0010$) and the combined outer-plus-distal compartment (adjusted $p = 1.31 \times 10^{-5}$). The core-like region also showed higher expression than the combined outer-plus-distal compartment (adjusted $p = 0.0039$; Fig. 1H).

We next examined the transcriptional programme accompanying this spatial pattern. A predefined HIF-1 response score was calculated from 25 canonical downstream genes. The score showed a peri-lesional distribution that closely paralleled *Hif1a* expression (Fig. 1G). Mean scores were -0.311, 0.156, 0.122 and 0.025 in the core-like, inner peri-lesional, outer peri-lesional and distal regions, respectively. The score was higher in the inner peri-lesional layer than in the core-like region (adjusted $p = 2.83 \times 10^{-10}$; Fig. 1I). Representative genes involved in oxygen sensing, glucose metabolism, vascular remodelling and stress adaptation, including *Angptl4*, *Egln3*, *Plod1*, *Hk2*, *Adm*, *Ldha*, *Slc2a1*, *Pdk1* and *Vegfa*, showed positive regional changes towards the putative penumbra (Fig. S1I). Region-standardized expression further showed coordinated changes in multiple canonical HIF-1 downstream genes across the lesion-associated compartments (Fig. S1C).

We then examined the temporal and cross-model distribution of *Hif1a*. Spatial expression changed across the sham, day-2, day-10 and day-21 ET-1 sections, with prominent lesion-associated patterns during the acute and subacute phases (Fig. S1B). KEGG analysis identified 95 enriched pathways on day 2, including six containing *Hif1a*, and 30 enriched pathways on day 10, including five containing *Hif1a*. No pathways containing *Hif1a* met the prespecified enrichment threshold on day 21 (Fig. S1H).

Independent stroke datasets showed similar lesion-associated spatial patterns. In the photothrombotic dataset, *Hif1a* was enriched in proximal peri-infarct tissue relative to the infarct core and more distal peri-infarct regions (Fig. S1D). In the MCAO-reperfusion dataset, lesion-associated *Hif1a* expression was observed in the ipsilateral hemisphere together with spatial *Vegfa* expression (Fig. S1E).

Finally, we examined HIF-1α localisation at the protein level in an independent p-MCAO model. At 8 h after modelling, HIF-1α immunoreactivity was prominent in proximal peri-lesional tissue adjacent to the infarct core, whereas GFAP showed a distinct and broader lesion-associated distribution (Fig. 1J). Quantification further showed a significant difference between the HIF-1α- and GFAP-immunoreactive areas (Fig. S1J).

Together, regional *Hif1a* enrichment, concordant HIF-1-associated transcriptional activity, temporal and cross-model spatial patterns, and protein-level localisation converged on HIF-1α as a candidate for ligand development.

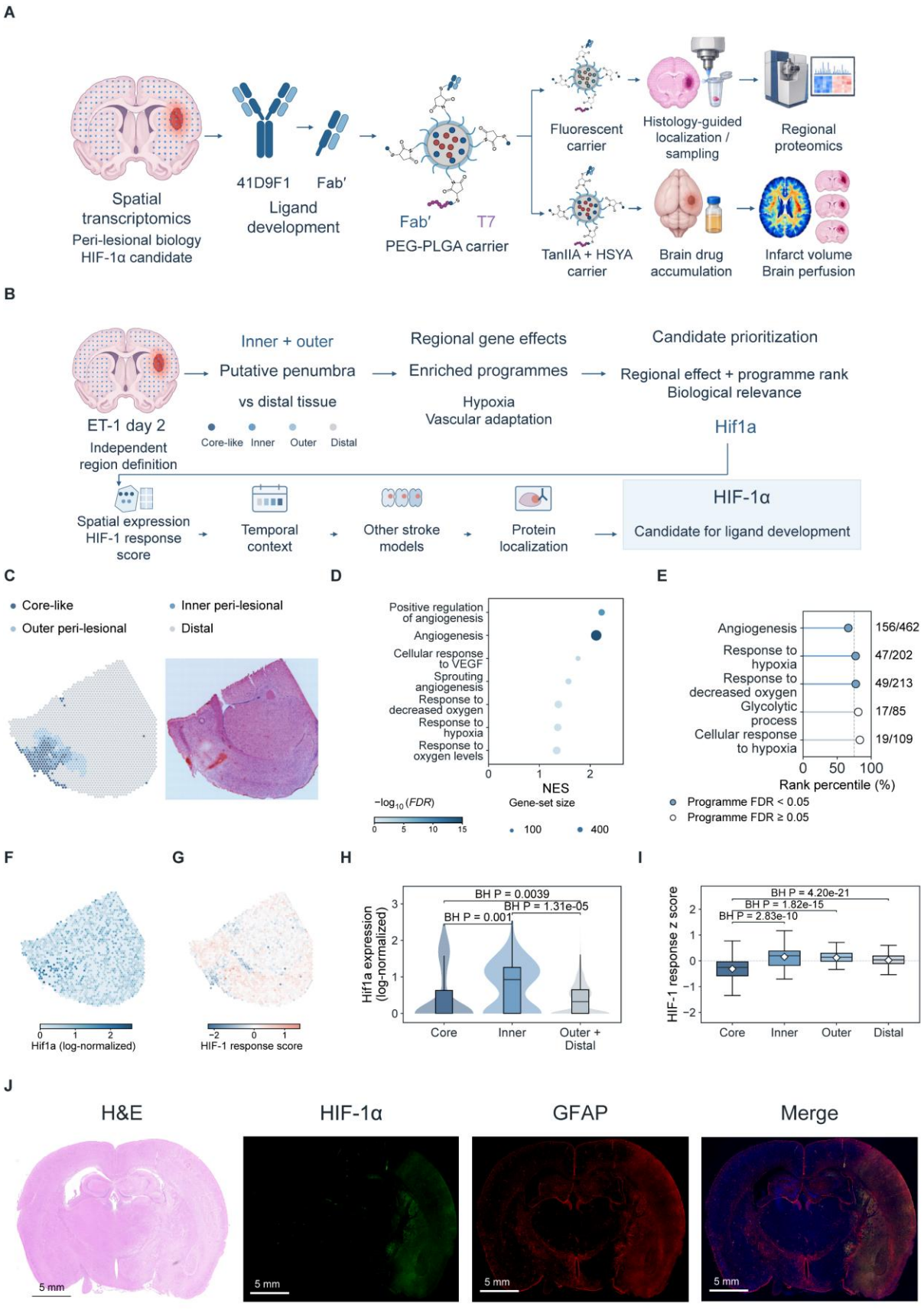

Fig. 1 Spatial and biological analyses prioritize HIF-1α for ligand development. (A) Overall workflow linking spatial candidate discovery, 41D9F1/Fab′ development and dual-functionalized nanocarriers with fluorescence-guided regional proteomics or dual-drug delivery. (B) Candidate prioritization and spatial evaluation. (C) Core-like, inner peri-lesional, outer peri-lesional and distal regions in the day-2 ET-1 section and corresponding H&E

image; inner and outer regions together define the putative penumbra. (D) Preranked Gene Ontology biological-process enrichment. Dot size, gene-set size; colour, $-\log_{10}$(FDR). FDR was controlled using the Benjamini–Hochberg procedure. (E) Within-programme rank of *Hif1a*; filled and open symbols indicate programme FDR < 0.05 and ≥ 0.05, respectively. (F,G) Spatial maps of log-normalized *Hif1a* expression (F) and the predefined 25-gene HIF-1 response score excluding *Hif1a* (G). (H) *Hif1a* expression in the core-like, inner peri-lesional and combined outer-plus-distal compartments. (I) HIF-1 response scores across all four regions; diamonds indicate regional means. Core, core-like; Inner and Outer, inner and outer peri-lesional regions; Distal, distal tissue. Panels C, H and I use the same day-2 region assignments. Comparisons in H and I used two-sided Wilcoxon rank-sum tests at spot level, with Benjamini–Hochberg adjustment across the three comparisons in each panel. Spots are not independent animal replicates. (J) H&E and whole-section immunofluorescence at 8 h after p-MCAO. Green, HIF-1α; red, GFAP; blue, DAPI. Explanatory schematic elements were prepared with assistance from ChatGPT (OpenAI) and subsequently edited and checked by the authors.

41D9F1 recognizes HIF-1α and Pro564-adjacent peptides

Following the prioritization of HIF-1α, we generated a monoclonal antibody against its oxygen-dependent degradation domain (ODD). A recombinant rat HIF-1α fragment spanning residues 380-585 was used as the immunogen. Two overlapping peptides covering the region adjacent to Pro564 were designed for secondary screening (Fig. 2A). This approach combined antibody generation against the ODD-containing fragment with subsequent screening for recognition of the Pro564-adjacent region.

Immunization produced a dilution-dependent serum response to the recombinant HIF-1α antigen (Fig. 2B). Initial hybridoma screening yielded 39 candidate clones, from which 32 positive monoclonal lines were obtained after subcloning. Eight clones with strong antigen reactivity underwent further subcloning and characterization. Candidate selection incorporated binding to the recombinant antigen and overlapping peptides, cellular staining, and western blot recognition. These analyses led to the selection of 41D9F1 (Fig. 2A).

ELISA showed that 41D9F1 bound the recombinant HIF-1α fragment and both Pro564-adjacent peptides (Fig. 2C). The binding signal for peptide 1 approached that of the recombinant antigen, whereas peptide 2 produced a lower signal. Recognition of both overlapping peptides supported antibody reactivity towards the Pro564-adjacent region of the ODD.

We next examined recognition of endogenous HIF-1α. Flow cytometry of fixed and permeabilized U87 MG and HeLa cells showed that nearly all cells were positive after staining with 41D9F1, whereas unstained and mIgG-FITC controls showed low background signals (Fig. 2D,E). Western blotting detected an HIF-1α-immunoreactive band at approximately 130 kDa in several cell lysates (Fig. 2F). These findings extended the binding results from purified antigens to HIF-1α in cellular samples.

We then assessed the distribution of 41D9F1 following local administration to infarct-associated brain tissue. Free FITC or FITC-labelled 41D9F1 (41D9F1-FITC) was injected into the peri-infarct cortex, and brain fluorescence was examined 6 h later. Whole-brain radiant efficiency was comparable between the two groups. However, the dissected infarct region showed higher fluorescence after 41D9F1-FITC administration than after free FITC (Fig. 2G,H). The labelled antibody therefore showed greater local retention within infarct-associated tissue.

We further examined HIF-1α protein abundance after treatment with the intact 41D9F1 monoclonal antibody. In the non-ischaemic experiment, brain HIF-1α concentrations were comparable among untreated controls and sham-operated rats receiving intravenous PBS or intact 41D9F1 (Fig. S2A). In MCAO rats, western blotting showed higher HIF-1α protein abundance after intact 41D9F1 treatment than after PBS treatment (Fig. S2B). Densitometric analysis showed a corresponding increase in the HIF-1α/β-actin ratio (Fig. S2C).

These results identified 41D9F1 as an HIF-1α-binding monoclonal antibody with reactivity towards the Pro564-adjacent region. Its recognition of endogenous HIF-1α, local retention in infarct-associated tissue, and association with increased HIF-1α abundance in MCAO rats supported its selection for subsequent Fab′-based ligand development.

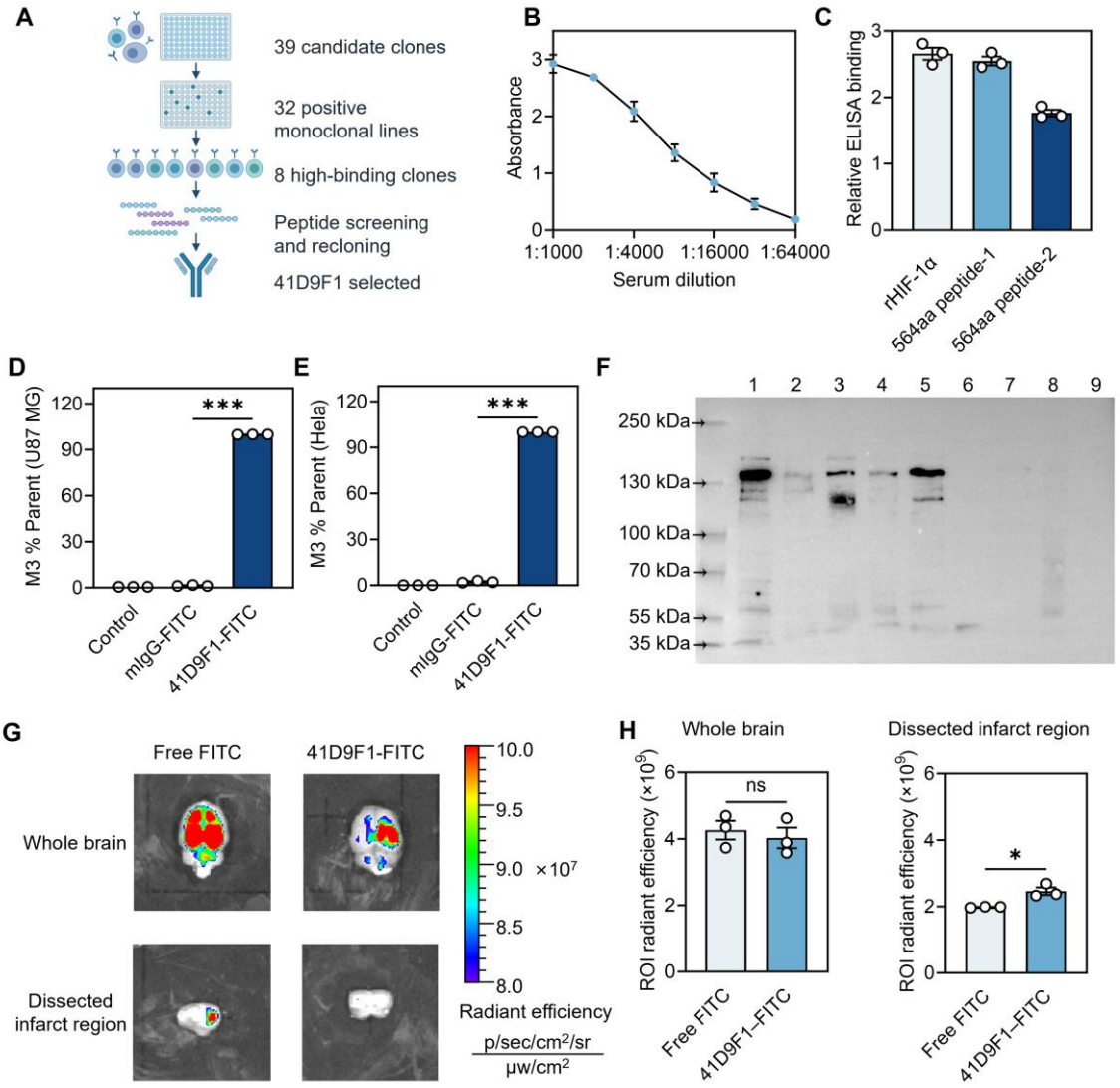

Fig. 2 Generation and characterization of the HIF-1α-binding monoclonal antibody 41D9F1. (A) Hybridoma-screening and selection workflow. Screening of 39 candidate clones, repeated subcloning and peptide reactivity testing led to selection of 41D9F1. (B) Serum titration against the recombinant HIF-1α antigen after immunization (n = 3). (C) ELISA binding of 41D9F1 to recombinant HIF-1α residues 380-585 and the two Pro564-adjacent peptides (n = 3). (D,E) Flow-cytometric analysis of fixed and permeabilized U87 MG and HeLa cells stained with 41D9F1 (n = 3). (F) Western blot analysis of HIF-1α recognition. Lanes 1–9: DMOG-treated HeLa, HepG2, U87 and SH-SY5Y cells; JK-1, MCF-7 and CP-R137 cells; and mouse and rat skeletal muscle, respectively. (G) Representative ex vivo fluorescence images of the whole brain (upper row) and dissected infarct region (lower row) 6 h after intracerebral administration of free FITC or 41D9F1-FITC. (H) Quantification of ROI radiant efficiency in whole brains and dissected infarct regions. Dots represent independent samples. Data are mean ± SD. *$p < 0.05$; ***$p < 0.001$; ns, not significant. Explanatory schematic elements were prepared with assistance from ChatGPT (OpenAI) and subsequently edited and checked by the authors.

Nanoparticle-conjugated Fab′ retains HIF-1α binding

We next incorporated the 41D9F1-derived Fab′ into a PEG-PLGA nanocarrier and evaluated its antigen-binding activity after surface conjugation. TanIIA and HSYA were co-loaded into PEG-PLGA nanoparticles by solvent diffusion and self-assembly. The 41D9F1-derived Fab′ was subsequently conjugated to the nanoparticle surface, followed by the addition of T7 peptide (Fig. 3A). The three formulations prepared for comparison were TanIIA/HSYA@PS, TanIIA/HSYA@T7-PS and TanIIA/HSYA@T7/HIF-PS, representing ligand-free, T7-functionalized and dual-functionalized nanoparticles, respectively. PS denotes the PEG-PLGA scaffold, T7 denotes the brain-targeting peptide, and HIF denotes the 41D9F1-derived HIF-1α-binding Fab′; the notation drug@carrier identifies the encapsulated payload and its carrier.

Nanoparticle tracking analysis showed X50 particle diameters of 109.60 ± 0.46, 128.33 ± 22.56 and 128.07 ± 16.84 nm for the three formulations, respectively (Table S1). Their corresponding ζ potentials were -40.65 ± 2.59, -33.60 ± 5.35 and -18.49 ± 3.93 mV. Particle-size distributions and transmission electron microscopy revealed predominantly spherical nanoparticles with well-defined boundaries (Fig. 3B-D). The three formulations also retained both drugs after purification. TanIIA encapsulation efficiencies ranged from 57.29% to 59.74%, with drug-loading contents of 2.240-2.333%. The corresponding values for HSYA were 21.96-24.38% and 0.871-0.966%, respectively (Table S1).

We then examined whether the nanoparticle-conjugated Fab′ retained HIF-1α recognition. SDS-PAGE showed a protein-associated band at approximately 50-55 kDa in T7/HIF-PS, whereas no corresponding band was detected in PS or T7-PS (Fig. S3). Antigen-binding activity was further assessed using HIF-1α-coated magnetic beads (Fig. 3E). Following incubation and washing, T7/HIF-PS showed markedly higher bead-associated fluorescence than PS and T7-PS (Fig. 3F). These results indicated that the 41D9F1-derived Fab′ retained the ability to bind HIF-1α after nanoparticle conjugation.

We next investigated the release behaviour of TanIIA and HSYA. Both free drugs were almost completely released within approximately 12 h, whereas encapsulation in PEG-PLGA nanoparticles delayed their release. At pH 7.4, cumulative release at 36 h reached approximately 50% for TanIIA and 80% for HSYA. Under acidic, lipase-containing conditions, these values increased to approximately 70%

and 95%, respectively (Fig. 3G-J). Similar release profiles were observed among the three nanoparticle formulations under the corresponding conditions.

These findings showed that the 41D9F1-derived Fab′ retained HIF-1α-binding activity after conjugation to PEG-PLGA nanoparticles. The resulting formulations also maintained dual-drug loading and comparable in vitro release behaviour, supporting their subsequent evaluation in brain delivery studies.

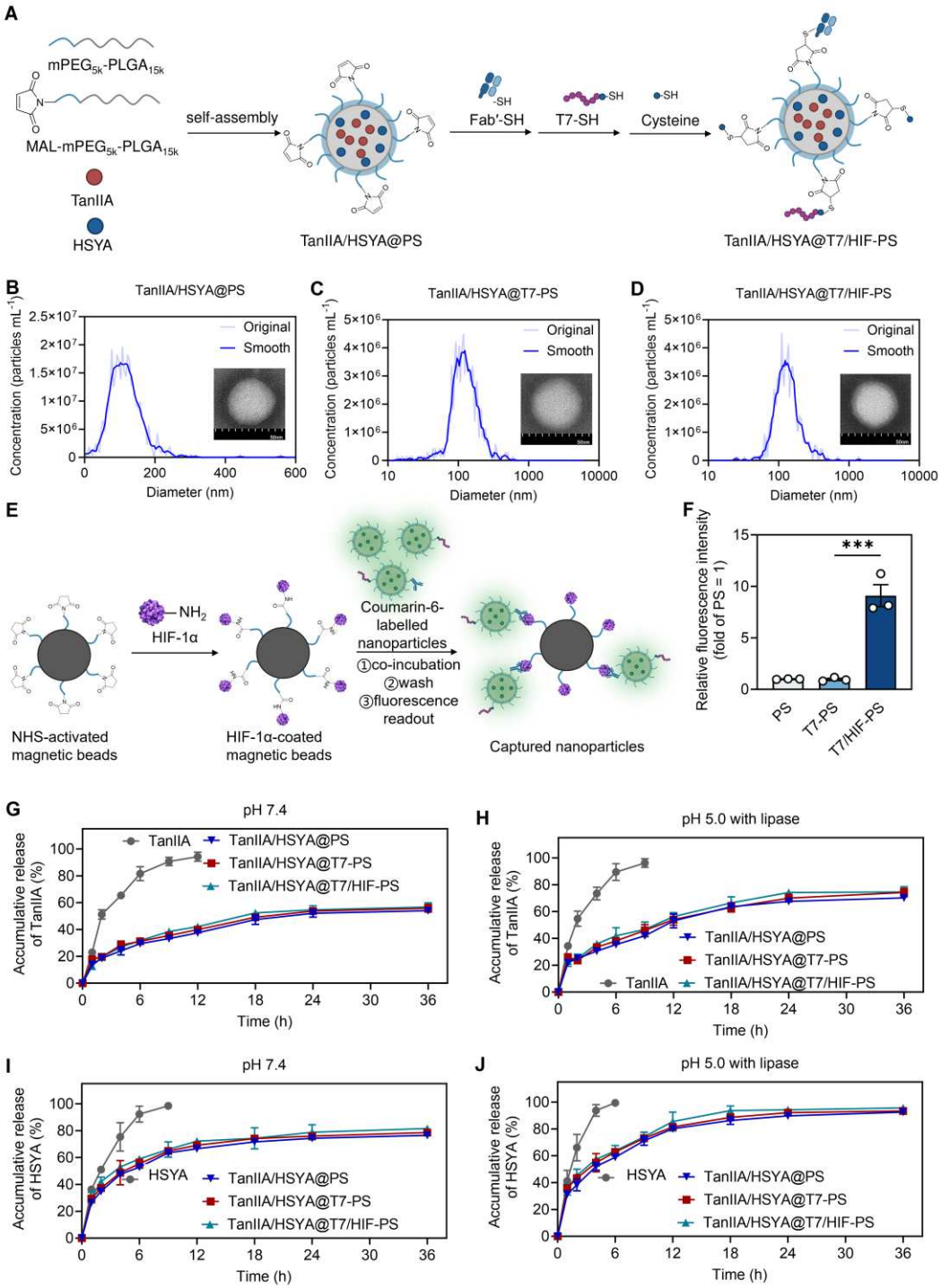

Fig. 3 Preparation, characterization and release of dual-drug PEG–PLGA nanoparticles. (A) Schematic illustration of nanoparticle preparation and sequential surface functionalization with 41D9F1-derived Fab′ and T7. (B-D) Particle-size distributions and representative transmission electron microscopy images of

TanIIA/HSYA@PS (B), TanIIA/HSYA@T7-PS (C) and TanIIA/HSYA@T7/HIF-PS (D). Scale bars, 50 nm. (E) Schematic illustration of the HIF-1α antigen-coated magnetic-bead capture assay. (F) Quantification of bead-associated fluorescence after incubation with coumarin-6-labelled PS, T7-PS or T7/HIF-PS, normalized to the PS group (n = 3). (G,H) Cumulative release of TanIIA at pH 7.4 (G) and pH 5.0 with lipase (H) (n = 3). (I,J) Cumulative release of HSYA under the corresponding conditions (n = 3). Dots represent independent samples. Data are mean ± SD. *** $p < 0.001$. Explanatory schematic elements were prepared with assistance from ChatGPT (OpenAI) and subsequently edited and checked by the authors.

Dual functionalization increases brain drug accumulation and cellular uptake under hypoxia

We next examined brain drug accumulation and cellular uptake using ligand-free nanoparticles, T7-functionalized nanoparticles and nanoparticles carrying both T7 and 41D9F1 Fab′. Following intravenous administration in p-MCAO rats, ex vivo imaging of perfused brains showed greater DiR fluorescence with T7-PS than with PS. T7/HIF-PS produced the highest brain-associated fluorescence signal (Fig. 4A,B). HPLC analysis showed a similar pattern for both drugs. Brain accumulation of TanIIA and HSYA increased from the ligand-free formulation to the T7-functionalized formulation and was highest with the dual-functionalized formulation (Fig. 4C,D). These results showed consistent changes in brain-associated fluorescence and drug accumulation across the three formulations.

We then examined cellular fluorescence under normoxic and hypoxic conditions. Fluorescence microscopy showed greater coumarin-6 signals in cells exposed to T7-functionalized nanoparticles than in those treated with PS. Under hypoxia, T7/HIF-PS produced the strongest cellular fluorescence, with signals distributed predominantly outside the nuclei (Fig. 4E). Quantification of background-corrected fluorescence per DAPI-positive cell showed a corresponding increase in cellular fluorescence associated with dual functionalization (Fig. 4F).

To characterize these differences further, we measured nanoparticle uptake in RBE4 brain microvascular endothelial cells and SH-SY5Y neuron-like cells by flow cytometry. Under normoxia, T7-PS and T7/HIF-PS showed higher uptake than PS in RBE4 cells, with similar signals between the two T7-functionalized formulations (Fig. 4G). Under hypoxia, uptake of T7/HIF-PS increased further and exceeded that of T7-PS (Fig. 4H). In SH-SY5Y cells, both T7-functionalized formulations increased

uptake relative to PS under normoxic and hypoxic conditions. However, the additional difference between T7-PS and T7/HIF-PS was less pronounced than in hypoxic RBE4 cells (Fig. 4I, 4J). The corresponding flow-cytometric histograms are shown in Fig. S4.

An additional comparison was performed in hypoxic RBE4 cells using PS, T7-PS, HIF-PS1, HIF-PS2 and T7/HIF-PS. The dual-functionalised formulation showed the highest uptake signal among these formulations. Treatment with CAY10585, an inhibitor of HIF-1α accumulation and HIF-1 transcriptional activity, reduced the fluorescence signal relative to T7/HIF-PS (Fig. 4K), suggesting that the enhanced uptake was at least partly dependent on HIF-1α availability. The corresponding flow-cytometric histograms are provided in Fig. S5.

These results showed increased brain-associated accumulation of both TanIIA and HSYA following dual functionalization. At the cellular level, the additional uptake advantage of T7/HIF-PS was most evident in RBE4 cells under hypoxia.

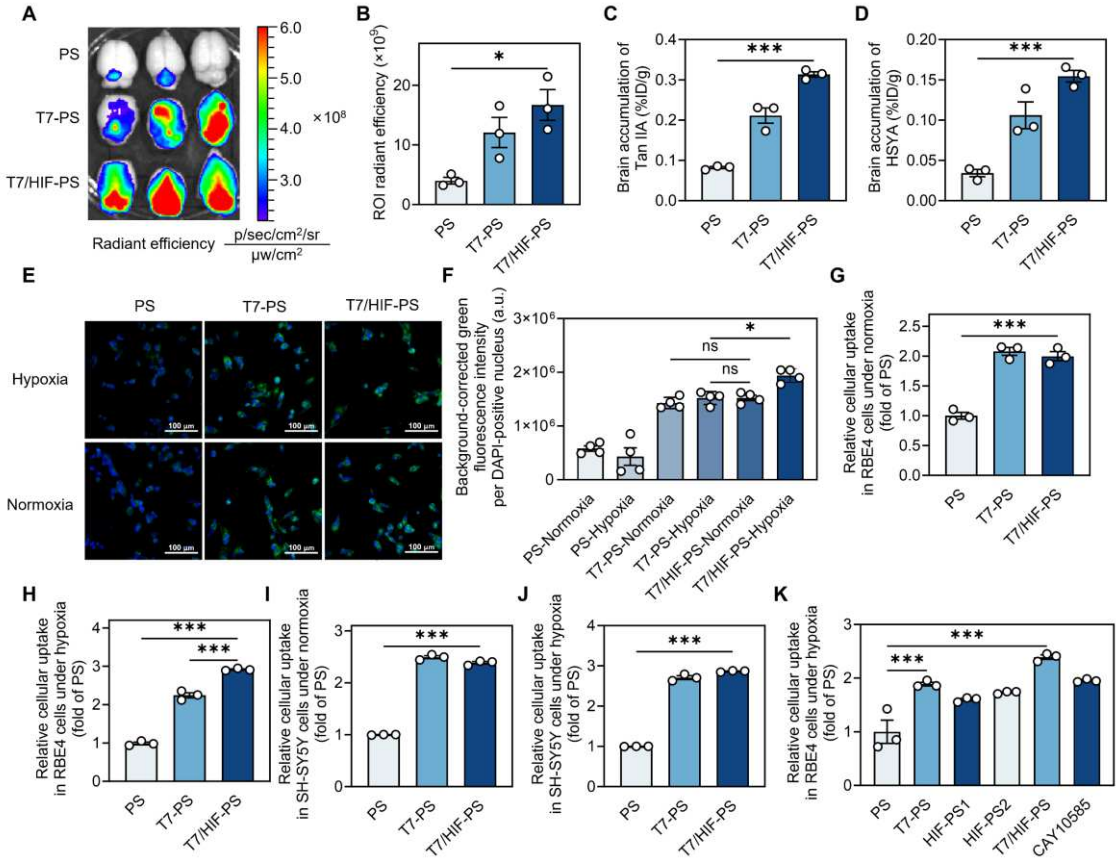

Fig. 4 Dual functionalization increases brain drug accumulation and cellular uptake under hypoxia. (A) Representative ex vivo fluorescence images of perfused brains from p-MCAO rats 6 h after intravenous administration of DiR-labelled PS, T7-PS or T7/HIF-PS. (B) Quantification of brain-associated radiant

efficiency (n = 3). (C,D) HPLC quantification of TanIIA (C) and HSYA (D) accumulation in brain tissue, expressed as percentage of injected dose per gram of tissue (%ID/g; n = 3). (E) Representative fluorescence images of cells exposed to coumarin-6-labelled PS, T7-PS or T7/HIF-PS under normoxic or hypoxic conditions. Green, coumarin-6; blue, DAPI. (F) Background-corrected cellular fluorescence intensity per DAPI-positive cell (n = 4). (G-J) Relative uptake of coumarin-6-labelled nanoparticles measured by flow cytometry in RBE4 cells under normoxia (G) and hypoxia (H), and SH-SY5Y cells under normoxia (I) and hypoxia (J) (n = 3). (K) Relative nanoparticle uptake in hypoxic RBE4 cells following treatment with different ligand-functionalized formulations and the CAY10585-labelled condition (n = 3). Dots represent individual measurements. Data are mean ± SD. * $p < 0.05$; *** $p < 0.001$; ns, not significant.

Fab′-functionalized nanoparticles guide regional proteomic profiling of the ischaemic brain

We next examined the regional distribution of Fab′-functionalized nanoparticles in the ischaemic brain and used their fluorescence signals to guide regional proteomic analysis. DiI-labelled nanoparticles were administered intravenously at 2 h after p-MCAO, and brains were collected 6 h later. Serial cryosections were prepared for fluorescence imaging, H&E staining and laser microdissection. DiI fluorescence and corresponding histological features were used for regional delineation through semiautomated image analysis and manual refinement (Fig. 5A).

Whole-section fluorescence imaging showed distinct distribution patterns among the control, T7-PS and T7/HIF-PS groups (Fig. 5C). In the p-MCAO model, T7/HIF-PS showed more prominent DiI fluorescence in peri-infarct cortical tissue than T7-PS. Comparison with adjacent H&E sections revealed corresponding regional differences in tissue morphology. Peri-infarct tissue with relatively high DiI fluorescence and preserved tissue architecture was designated the putative penumbra zone (PZ). The infarct region (IR) was identified by disrupted tissue architecture and reduced cellular density, while cortical tissue with low fluorescence and relatively preserved morphology was designated the non-infarct region (NIR). These spatial features guided regional delineation and subsequent tissue sampling.

The resulting regional masks were aligned with the corresponding cryosections for laser microdissection. Equal cumulative tissue areas were collected from NIR, PZ and IR within each animal, followed by regional proteomic analysis (Fig. 5A). Principal component analysis showed separation among the three

regional proteomes. PC1 and PC2 accounted for 31.9% and 19.3% of the total variance, respectively (Fig. 5B).

We next examined regional protein abundance patterns. A total of 1,305 proteins met the differential-abundance criteria in at least one pairwise regional comparison ($p < 0.05$ and $|\log_2 \text{fold change}| > 0.585$). Clustering of their standardized regional mean abundances identified five distinct expression patterns (Fig. 5D). Cluster 1 (247 proteins) increased progressively from NIR to PZ and IR and was enriched in ribonucleoprotein complex biogenesis, ribosome biogenesis, and proteasome- and lysosome-related pathways. Cluster 3 (302 proteins) showed its lowest abundance in PZ and highest abundance in IR, with enrichment in intermediate filament organization, cell adhesion, and complement and coagulation cascades.

Cluster 2 (335 proteins) showed relatively high abundance in NIR and PZ, followed by a marked reduction in IR. This cluster was enriched in cellular respiration, aerobic respiration and oxidative phosphorylation. Cluster 4 (191 proteins) decreased progressively from NIR to PZ and IR and was associated with synaptic vesicle transport, synaptic vesicle cycling, postsynaptic organization and glutamatergic synapse pathways. Cluster 5 (230 proteins) showed its highest abundance in PZ and included proteins associated with Golgi vesicle transport, mitochondrial transport, membrane organization, autophagy, mitophagy and endocytosis (Fig. 5D).

We further examined selected glycolysis- and autophagy-associated proteins across the three regions (Fig. S6). HK1 abundance decreased by 0.579 and 1.267 $\log_2$ units in PZ and IR relative to NIR, respectively. PGK1 showed a similar downward mean trend, with lower abundance in IR than in NIR. In contrast, LC3A and LC3B reached their highest mean abundances in PZ, increasing by 0.615 and 1.811 $\log_2$ units relative to NIR, respectively. These changes were consistent with the regional patterns identified by proteomic clustering.

These findings showed that DiI-labelled T7/HIF-PS exhibited peri-infarct enrichment and that its fluorescence distribution could guide regional tissue sampling. Proteomic analysis further identified distinct molecular profiles across the three cortical regions. The putative penumbra was characterized by

relative retention of respiration-associated proteins and enrichment of intracellular trafficking and autophagy-associated proteins, together with reduced abundance of synaptic components.

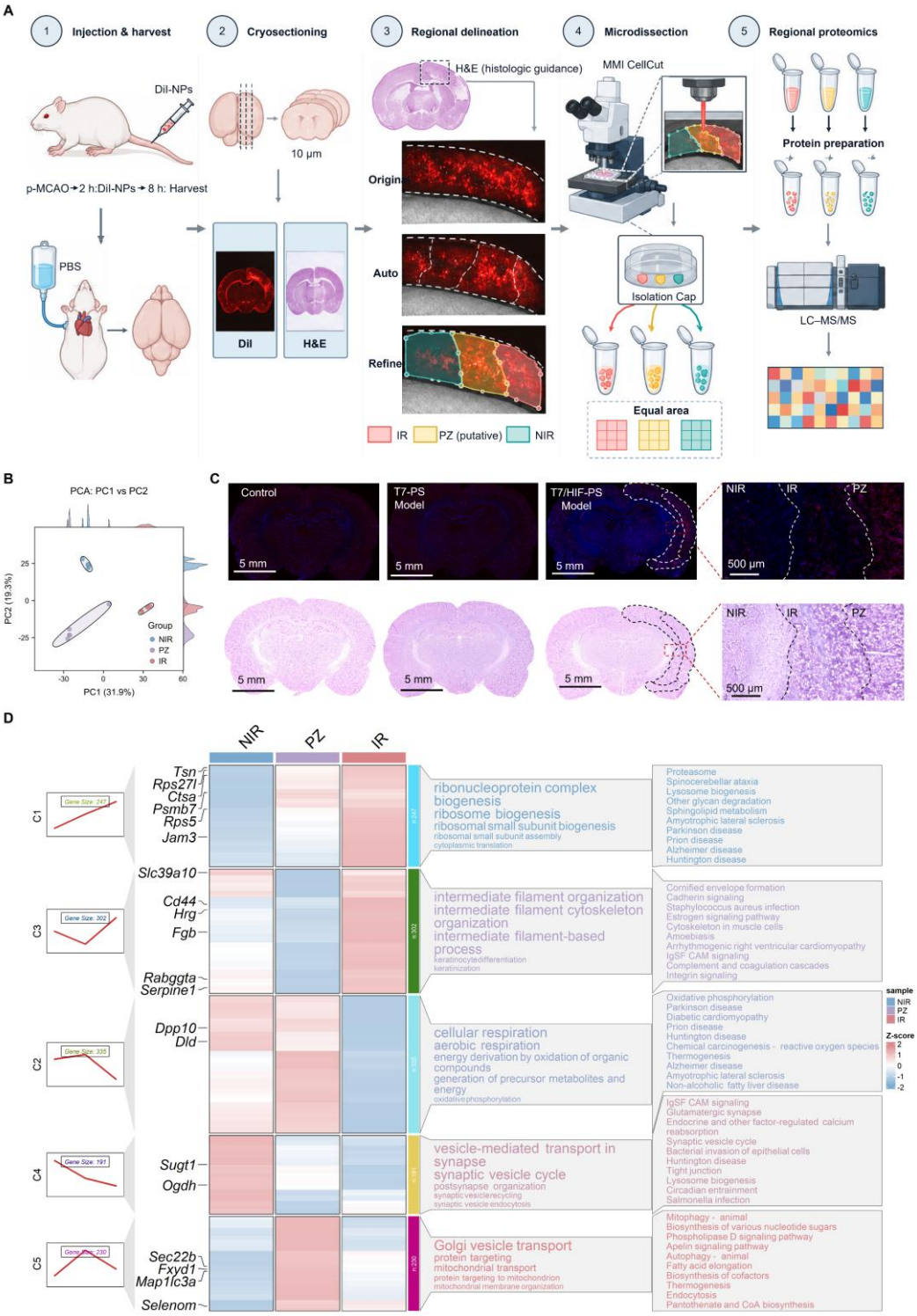

Fig. 5 Regional localization of Fab′-functionalized nanoparticles and cortical proteomic profiles. (A) Schematic illustration of DiI-labelled nanoparticle administration, cryosectioning, fluorescence- and histology-guided regional delineation, laser microdissection and proteomic analysis. (B) Principal component analysis of regional proteomes from the non-infarct region (NIR), putative penumbra zone (PZ) and infarct region (IR) of the ipsilateral cerebral cortex (n = 5 per region). PC1 and PC2 explain 31.9% and 19.3% of the total variance,

respectively. (C) Representative DiI fluorescence images and corresponding H&E-stained sections from the control, T7-PS and T7/HIF-PS groups (n = 5 per group). Dashed lines indicate the delineated cortical regions. Scale bars, 5 mm and 500 μm, as indicated. (D) Five clusters of region-associated proteins identified using $p <$ 0.05 and $|\log_2 \text{fold change}| > 0.585$ in at least one pairwise regional comparison. The panel shows standardized regional mean protein abundances, representative proteins and corresponding Gene Ontology biological-process and KEGG pathway annotations. The five clusters comprise 247, 302, 335, 191 and 230 proteins for C1, C3, C2, C4 and C5, respectively. Explanatory schematic elements were prepared with assistance from ChatGPT (OpenAI) and subsequently edited and checked by the authors.

Dual-drug nanoparticles reduce acute infarct volume and alter brain protein profiles

Following the characterization of brain accumulation and peri-infarct localization, we evaluated the acute therapeutic effects of the nanoparticle formulations in p-MCAO rats. The experimental groups allowed comparison of unmodified PS, drug-free T7/HIF-PS, the two single-drug formulations and the dual-drug formulation against sham-operated and model controls. Treatments were administered intravenously 2 h after modelling, and acute endpoints were assessed 6 h later. A subset of animals underwent laser speckle contrast imaging before brain collection for TTC staining (Fig. 6A).

TTC staining showed extensive unstained regions in the Model and PS groups, whereas these regions were smaller in animals receiving T7/HIF-PS or the drug-loaded formulations (Fig. 6B). Oedema-corrected infarct volume was 40.45 ± 1.83% in the Model group and 38.41 ± 3.38% in the PS group, with no significant difference between them. By comparison, drug-free T7/HIF-PS reduced infarct volume to 27.38 ± 0.55%, showing a tissue-level response to the drug-free functionalized carrier. Lower mean infarct volumes were observed with TanIIA@T7/HIF-PS and HSYA@T7/HIF-PS, at 19.94 ± 4.97% and 22.22 ± 3.92%, respectively. The dual-drug formulation produced the lowest mean value, at 12.50 ± 2.21% (Fig. 6C). The groupwise pattern therefore showed a reduction associated with the drug-free functionalized carrier and a more pronounced reduction in the drug-loaded groups.

We next examined whether the reduction in infarct volume was accompanied by changes in cerebral perfusion. Laser speckle contrast imaging showed markedly lower perfusion signals in the Model group than in the Control group. Higher signals were observed after treatment with either drug-free T7/HIF-PS

or TanIIA/HSYA@T7/HIF-PS (Fig. 6D). Mean cerebral perfusion decreased from 1458.8 ± 87.0 perfusion units (PU) in the Control group to 415.7 ± 20.7 PU in the Model group. The corresponding values were 731.4 ± 57.7 PU with T7/HIF-PS and 856.8 ± 57.7 PU with the dual-drug formulation (Fig. 6E). Across the groups examined, lower infarct burden was thus accompanied by higher cerebral perfusion, providing concordant tissue-level and physiological evidence of an acute treatment response.

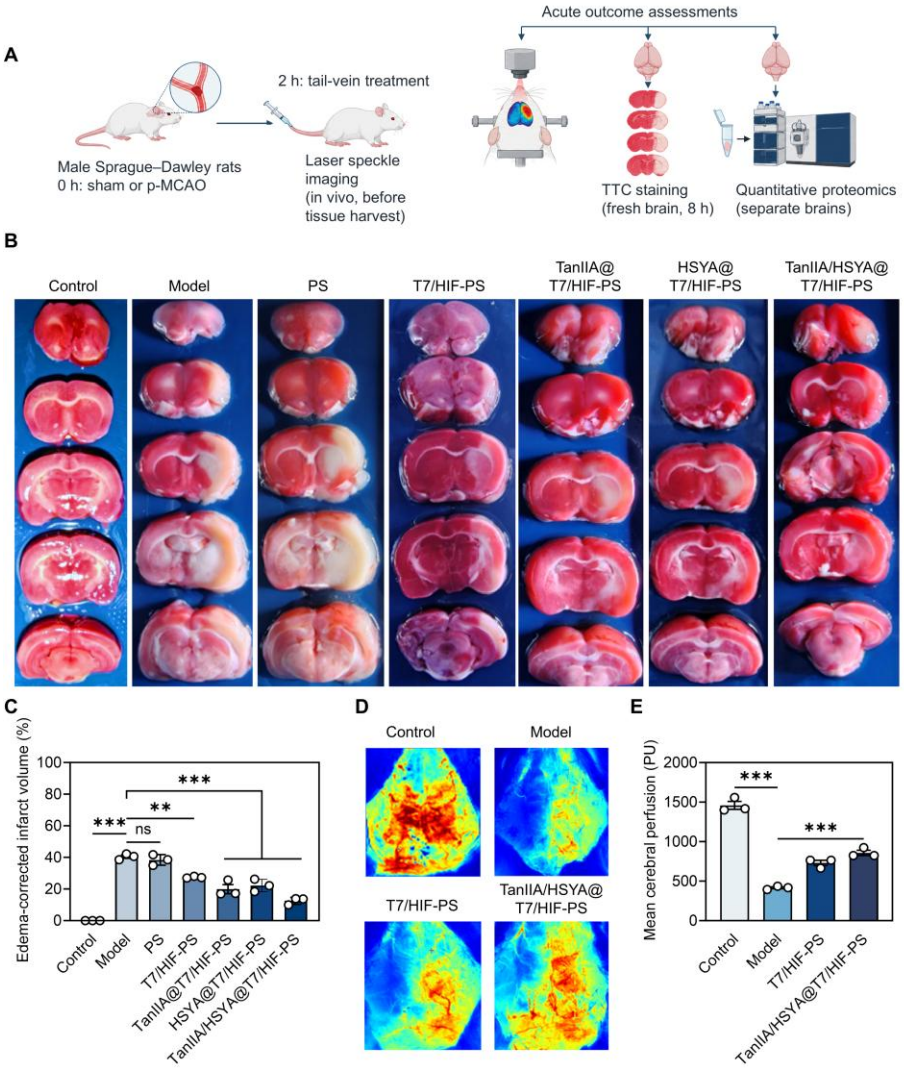

Fig. 6 Acute therapeutic effects of dual-drug nanoparticles in ischaemic stroke. (A) Experimental timeline for acute therapeutic evaluation. Rats received intravenous treatment 2 h after p-MCAO, and endpoints were assessed 6 h later. A subset of animals underwent laser speckle contrast imaging before brain collection for TTC staining. (B) Representative TTC-stained coronal brain sections from the Control, Model, PS, T7/HIF-PS, TanIIA@T7/HIF-PS, HSYA@T7/HIF-PS and TanIIA/HSYA@T7/HIF-PS groups. The Control group underwent sham surgery, and the Model group underwent p-MCAO; both received saline. PS and T7/HIF-PS denote drug-free formulations. (C) Quantification of oedema-corrected infarct volume, expressed as a percentage of the contralateral hemisphere (n = 3 per group). (D) Representative laser speckle contrast images from the

Control, Model, T7/HIF-PS and TanIIA/HSYA@T7/HIF-PS groups. (E) Mean cerebral perfusion in the ipsilateral middle cerebral artery territory, expressed in perfusion units (PU; $n = 3$ per group). Dots represent individual measurements. Data are mean ± SD. $^{**}p < 0.01$; $^{***}p < 0.001$; ns, not significant, for the indicated comparisons. Explanatory schematic elements were prepared with assistance from ChatGPT (OpenAI) and subsequently edited and checked by the authors.

We then used quantitative proteomics to examine how the brain protein profiles differed among the treatment groups. Principal component analysis separated the experimental groups, with PC1 and PC2 explaining 44.7% and 18.4% of the total variance, respectively. The HSYA and dual-drug groups were positioned towards the Control group along PC1, whereas the TanIIA group remained closer to the Model group on this axis (Fig. 7A). The treatments therefore produced distinguishable global protein-abundance patterns. The two monotherapy groups and the dual-drug group shared 148 proteins that met the differential-abundance criteria relative to the Model group (adjusted $p < 0.05$ and $|\log_2 \text{fold change}| > 1$). Another 163 proteins met these criteria only in the dual-drug comparison (Fig. 7B). These results identified both an overlapping set of treatment-responsive proteins and additional changes associated with the combined formulation.

To relate these treatment responses to the differences between control and ischaemic tissue, we compared the directions of protein-abundance changes relative to the Model group. Selected proteins showed concordant increases or decreases in the Control-versus-Model and dual-drug-versus-Model comparisons (Fig. 7C). Proteins labelled Ptma, Nsf and Nup85 were more abundant in both the Control and dual-drug groups than in the Model group. Conversely, Fn1, Crp and Tf were less abundant in both comparisons. Thus, within this selected protein subset, the dual-drug-associated changes opposed the direction of the Model-associated differences.

Coexpression analysis further organized the proteomic variation into turquoise and blue modules (Fig. 7D). These modules showed opposite correlation patterns across the experimental conditions. The turquoise module correlated positively with both the Control and combination-treatment groups, whereas the blue module correlated negatively with these groups. For combination treatment, the respective correlations were $r = 0.47$ ($p = 0.10$) and $r = -0.57$ ($p = 0.05$; Fig. 7E). Functional enrichment analysis

highlighted presynaptic endocytosis, synaptic vesicle recycling and dendrite development, together with cellular components including the presynaptic membrane, postsynaptic specialization and distal axon. Enriched pathways included the synaptic vesicle cycle and mTOR, phospholipase D and insulin signalling (Fig. 7F). These annotations identified synaptic organization, vesicular transport and associated signalling as prominent functional themes in the treatment-related protein changes.

Finally, an independent animal cohort was used to examine selected protein responses by western blotting (Fig. 7G). This experiment compared dual-drug formulations carrying T7 alone or both T7 and the 41D9F1-derived Fab′. The HIF-1α/β-actin ratio was 0.141 ± 0.034 in the Model group and 0.378 ± 0.017 after treatment with TanIIA/HSYA@T7-PS. The ratio increased further to 0.538 ± 0.049 with TanIIA/HSYA@T7/HIF-PS (Fig. 7H,J). The phospho-mTOR/total mTOR ratio was lower in the dual-functionalized dual-drug group than in the Model group (Fig. 7H,I). This comparison associated Fab′ functionalization with an additional increase in HIF-1α abundance in animals receiving the dual-drug formulation.

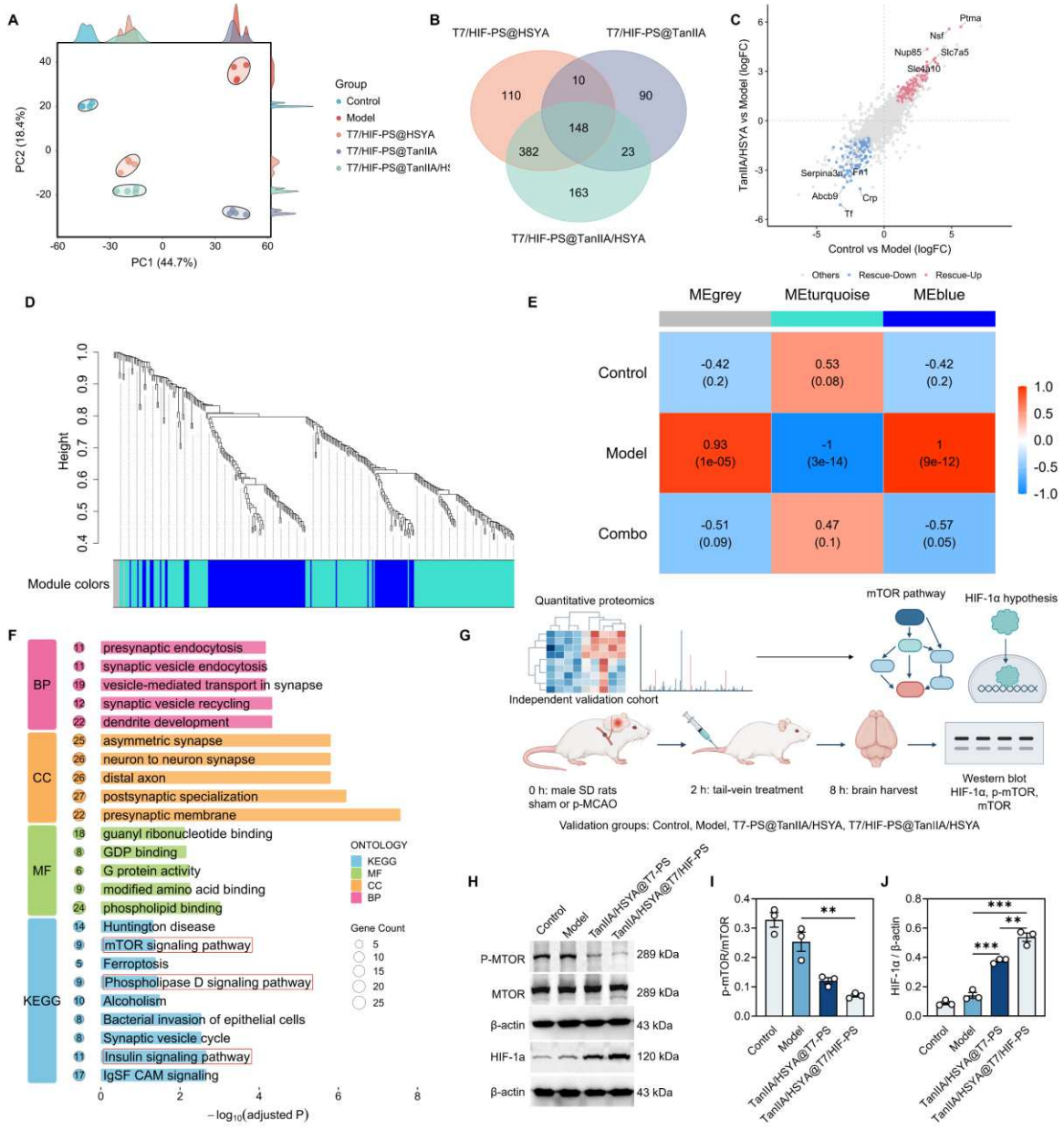

Fig. 7 Treatment-associated proteomic changes and selected protein responses in ischaemic brain tissue. (A) Principal component analysis of brain proteomes from the Control, Model, HSYA@T7/HIF-PS, TanIIA@T7/HIF-PS and TanIIA/HSYA@T7/HIF-PS groups. PC1 and PC2 explain 44.7% and 18.4% of the total variance, respectively. (B) Venn diagram showing the overlap of differentially abundant proteins in the two monotherapy groups and the dual-drug group relative to the Model group, using adjusted $p < 0.05$ and $|\log_2$ fold change$| > 1$. Differential protein abundance was analysed with limma in R 4.3.3, with Benjamini–Hochberg adjustment. (C) Comparison of protein-abundance changes in Control versus Model (horizontal axis) and dual-drug treatment versus Model (vertical axis). Pink and blue points indicate selected proteins showing concordant positive and negative changes, respectively; grey points indicate the remaining proteins. (D) Protein coexpression dendrogram and corresponding module assignments. (E) Pearson correlations between module eigengenes and the Control, Model and combination-treatment groups. Colours indicate correlation coefficients,

and values in parentheses indicate p values. (F) Gene Ontology and pathway over-representation analysis using hypergeometric tests with Benjamini–Hochberg adjustment. Bar length indicates $-\log_{10}$(adjusted p), and circle size indicates the number of annotated genes. BP, biological process; CC, cellular component; MF, molecular function. (G) Proteomics-informed experimental design for an independent four-group animal cohort used for western blot validation. Treatment was given intravenously 2 h after p-MCAO, with brain collection 6 h later. (H) Representative western blots of phospho-mTOR, total mTOR and HIF-1α in the Control, Model, TanIIA/HSYA@T7-PS and TanIIA/HSYA@T7/HIF-PS groups, with β-actin as the loading control. (I,J) Densitometric quantification of phospho-mTOR/mTOR (I) and HIF-1α/β-actin (J), with $n = 3$ per group. Dots represent individual measurements. Quantitative western blot data are mean ± SD. $^{**}p < 0.01$; $^{***}p < 0.001$, for the indicated comparisons. ChatGPT (OpenAI) assisted in preparing the schematic; the authors reviewed and edited it.

Discussion

We developed a strategy for penumbra-directed drug delivery guided by spatial transcriptomics and the biology of cerebral ischaemia, using an HIF-1α-binding Fab′ as the targeting ligand. Spatial studies have described distinct cellular and vascular states around ischaemic lesions [22,23]. Here, public spatial datasets were used to relate candidate expression to defined tissue compartments and hypoxia-associated programmes. Cross-model spatial patterns and protein localisation then supported HIF-1α prioritisation. This design links target selection to the regional tissue state that the delivery system is intended to address. We subsequently generated 41D9F1 against the oxygen-dependent degradation domain of HIF-1α and incorporated its Fab′ into an established T7-functionalised PEG-PLGA carrier. The carrier accommodated fluorescent labels and therapeutic payloads, allowing the targeting strategy to be examined through regional imaging, tissue sampling and drug delivery. This sequence translated spatial molecular information into a usable recognition ligand and enabled its evaluation in both regional tissue research and acute stroke treatment.

The validation experiments addressed antigen recognition, binding after conjugation and the response of the recognised protein. Recognition of recombinant HIF-1α, Pro564-adjacent peptides and endogenous protein supported the selection of 41D9F1. Antigen-coated magnetic beads demonstrated that nanoparticle-bound Fab′ retained binding activity, linking antibody characterisation to the final

formulation. Pro564 lies within the oxygen-dependent degradation region, where hydroxylation regulates recognition by the von Hippel-Lindau ubiquitin ligase complex [32]. Together with the increase in HIF-1α abundance following intact 41D9F1 treatment, recognition of this region suggests that antibody binding may enhance protein stability by limiting degradation. A stabilising effect could help sustain HIF-1α-associated adaptation to hypoxia and contribute to tissue protection. Because the drug-free dual-functionalised carrier also reduced infarct burden, ligand-associated biological effects deserve consideration when interpreting the response to the loaded formulation.

With fluorescent labelling, the formulation also served as a guide for regional tissue sampling. Peri-infarct fluorescence corresponded to morphological differences on adjacent H&E sections and supplied a visible spatial reference for microdissection. Regional assessment is important because nanoparticles can accumulate in both the infarct core and penumbra after permanent MCAO [7]. Proteomic analysis showed that the sampled compartments had distinct molecular profiles. In the putative penumbra, respiration-associated proteins were relatively retained compared with the infarct region, whereas synaptic components were reduced relative to non-infarct tissue. Proteins associated with intracellular trafficking and autophagy showed regional enrichment. This combination is consistent with tissue undergoing injury-associated remodelling while retaining components of energy metabolism. The molecular differences therefore support the biological relevance of the sampled compartments and the use of fluorescence with histology to guide collection. By linking carrier localisation to regional sampling and protein analysis, this application provides a practical means of examining the molecular heterogeneity of the ischaemic brain.

Loading TanIIA and HSYA tested the therapeutic application of this strategy in permanent MCAO. Reduced infarct volume and higher cerebral perfusion provided complementary evidence of acute benefit. The drug-free dual-functionalised carrier also showed activity, while the dual-drug formulation produced the lowest mean infarct volume. These comparisons identify carrier composition and payload selection as relevant variables in treatment development. Increased brain concentrations of both drugs support the delivery component of this response. Treatment proteomics associated the intervention with synaptic organisation, vesicular transport and related signalling processes. These findings overlap with functional

themes identified in regional profiling and suggest that the treatment response involves processes altered across the ischaemic tissue. In an independent cohort, higher HIF-1α abundance with the Fab′-functionalised formulation than with its T7-only counterpart provided further evidence of a ligand-associated protein response. Together, these results support evaluating regional delivery and biological activity when optimising the formulation.

The Fab′ could be adapted for fluorescent probes or carriers bearing other therapeutic agents. Coupling regional tracing with cell-type analysis and spatial profiling would extend its use to studies of injury progression and treatment responses. HIF-1α is intracellular, and the site and timing of its engagement by carrier-bound Fab′ remain unresolved. Direct measurements of protein turnover and transcriptional output are also needed to determine whether binding stabilises HIF-1α and sustains its function. At the tissue level, the putative penumbra was defined using fluorescence and morphology. Independent measures of perfusion and viability, combined with regional quantification of the actual payload, would determine how localisation relates to effective exposure and tissue outcome. Examining these relationships across disease stages and reperfusion conditions would guide ligand presentation, carrier selection and dosing windows.

Conclusions

We developed a strategy for penumbra-directed drug delivery guided by spatial transcriptomics and ischaemic tissue biology. The 41D9F1-derived Fab′ retained HIF-1α recognition after conjugation to T7-functionalised PEG-PLGA nanoparticles. Fluorescence combined with histology guided regional tissue sampling, and proteomics supported molecular differences among the sampled compartments. The dual-functionalised formulation increased brain drug accumulation, while the TanIIA/HSYA-loaded formulation reduced acute infarct volume and improved cerebral perfusion. Treatment was also associated with increased HIF-1α abundance. These findings support complementary applications of this strategy in regional biological studies and therapeutic delivery in experimental ischaemic stroke.

Supplementary information

Additional file 1. Supplementary information (.docx). Spatial transcriptomic and immunofluorescence analyses; effects of intact 41D9F1 on HIF-1α abundance; SDS–PAGE and flow-cytometric analyses; regional protein abundance profiles; nanoparticle physicochemical properties and drug-loading characteristics. Includes Figs. S1–S6 and Table S1.

Declarations

Ethics approval and consent to participate

All animal procedures were approved by the Experimental Animal Ethics Committee of the Experimental Research Center, China Academy of Chinese Medical Sciences (approval no. ERCCACMS21-2402-02).

Consent for publication

Not applicable.

Availability of data and materials

Processed data supporting the conclusions are provided in the main text and Additional file 1. Sources of publicly available spatial transcriptomic data are listed in Methods. The raw proteomic mass-spectrometry data have been deposited in ProteomeXchange under accession number PXD082896. Additional information is available from the corresponding author upon reasonable request.

Competing interests

The authors declare no competing interests.

Funding

This work was supported by the National Natural Science Foundation of China (82174238), the Beijing Natural Science Foundation (7242254), the National Natural Science Foundation of China (32595501), the Scientific and Technological Innovation Project of the China Academy of Chinese Medical Sciences (NLTL2025011), the Key Laboratory of Dunhuang Medicine, Ministry of Education (DHYX25-12), and the Fundamental Research Funds for the Central Public Welfare Research Institutes

(XTCX2023001, ZZ13-YQ-080). The funding sources had no role in study design; data collection, analysis or interpretation; manuscript preparation; or the decision to submit the article for publication.

Authors' contributions

Yusheng Zhang: Methodology, Investigation, Data curation, Formal analysis, Writing – original draft. Hong Wang: Methodology, Investigation, Data curation, Writing – original draft. Yiwan Geng: Methodology, Investigation. Zhiguo Lu: Resources, Writing – review & editing. Shaoqi Song: Visualization. Jie Wang: Formal analysis. Qing Wang: Writing – review & editing. Xin Zhang: Supervision, Writing – review & editing. Hongjun Yang: Project administration, Funding acquisition. Xianyu Li: Conceptualization, Writing – review & editing, Project administration, Funding acquisition. Yusheng Zhang, Hong Wang and Yiwan Geng contributed equally to this work. All authors reviewed and approved the final manuscript.

Acknowledgements

Not applicable.

References

1. Astrup J, Siesjö BK, Symon L. Thresholds in cerebral ischemia - the ischemic penumbra. Stroke. 1981;12:723–725. https://doi.org/10.1161/01.str.12.6.723

2. Lo EH, Dalkara T, Moskowitz MA. Mechanisms, challenges and opportunities in stroke. Nat Rev Neurosci. 2003;4:399–415. https://doi.org/10.1038/nrn1106

3. Heiss WD. The ischemic penumbra: how does tissue injury evolve? Ann N Y Acad Sci. 2012;1268:26–34. https://doi.org/10.1111/j.1749-6632.2012.06668.x

4. Baron JC. Protecting the ischaemic penumbra as an adjunct to thrombectomy for acute stroke. Nat Rev Neurol. 2018;14:325–337. https://doi.org/10.1038/s41582-018-0002-2

5. Campbell BCV, Khatri P. Stroke. Lancet. 2020;396:129–142. https://doi.org/10.1016/s0140-6736(20)31179-x

6. Thompson BJ, Ronaldson PT. Drug delivery to the ischemic brain. Adv Pharmacol. 2014;71:165–202. https://doi.org/10.1016/bs.apha.2014.06.013

992 7. Ishii T, Fukuta T, Agato Y, Oyama D, Yasuda N, Shimizu K, et al. Nanoparticles accumulate in ischemic core
993 and penumbra region even when cerebral perfusion is reduced. Biochem Biophys Res Commun.
994 2013;430:1201–1205. https://doi.org/10.1016/j.bbrc.2012.12.080
995 8. Zhang L, Chen D, Song D, Liu X, Zhang Y, Xu X, et al. Clinical and translational values of spatial
996 transcriptomics. Signal Transduct Target Ther. 2022;7:111. https://doi.org/10.1038/s41392-022-00960-w
997 9. Emmerich CH, Gamboa LM, Hofmann MCJ, Bonin-Andresen M, Arbach O, Schendel P, et al. Improving
998 target assessment in biomedical research: the GOT-IT recommendations. Nat Rev Drug Discov.
999 2021;20:64–81. https://doi.org/10.1038/s41573-020-0087-3
1000 10. Semenza GL. Hypoxia-inducible factors in physiology and medicine. Cell. 2012;148:399–408.
1001 https://doi.org/10.1016/j.cell.2012.01.021
1002 11. Lo EH. A new penumbra: transitioning from injury into repair after stroke. Nat Med. 2008;14:497–500.
1003 https://doi.org/10.1038/nm1735
1004 12. Iadecola C, Anrather J. The immunology of stroke: from mechanisms to translation. Nat Med. 2011;17:796–
1005 808. https://doi.org/10.1038/nm.2399
1006 13. Muro S. Challenges in design and characterization of ligand-targeted drug delivery systems. J Control
1007 Release. 2012;164:125–137. https://doi.org/10.1016/j.jconrel.2012.05.052
1008 14. Rao A, Barkley D, França GS, Yanai I. Exploring tissue architecture using spatial transcriptomics. Nature.
1009 2021;596:211–220. https://doi.org/10.1038/s41586-021-03634-9
1010 15. Gashaw I, Ellinghaus P, Sommer A, Asadullah K. What makes a good drug target? Drug Discov Today.
1011 2011;16:1037–1043. https://doi.org/10.1016/j.drudis.2011.09.007
1012 16. Moskowitz MA, Lo EH, Iadecola C. The science of stroke: mechanisms in search of treatments. Neuron.
1013 2010;67:181–198. https://doi.org/10.1016/j.neuron.2010.07.002
1014 17. Gidday JM. Cerebral preconditioning and ischaemic tolerance. Nat Rev Neurosci. 2006;7:437–448.
1015 https://doi.org/10.1038/nrn1927
1016 18. Sadekar S, Figueroa I, Tabrizi M. Antibody Drug Conjugates: Application of Quantitative Pharmacology in
1017 Modality Design and Target Selection. AAPS J. 2015;17:828–836. https://doi.org/10.1208/s12248-015-
1018 9766-0

19. Srinivasarao M, Galliford CV, Low PS. Principles in the design of ligand-targeted cancer therapeutics and imaging agents. Nat Rev Drug Discov. 2015;14:203–219. https://doi.org/10.1038/nrd4519

20. Srinivasarao M, Low PS. Ligand-Targeted Drug Delivery. Chem Rev. 2017;117:12133–12164. https://doi.org/10.1021/acs.chemrev.7b00013

21. Scott EY, Safarian N, Casasbuenas DL, Dryden M, Tockovska T, Ali S, et al. Integrating single-cell and spatially resolved transcriptomic strategies to survey the astrocyte response to stroke in male mice. Nat Commun. 2024;15:1584. https://doi.org/10.1038/s41467-024-45821-y

22. Han B, Zhou S, Zhang Y, Chen S, Xi W, Liu C, et al. Integrating spatial and single-cell transcriptomics to characterize the molecular and cellular architecture of the ischemic mouse brain. Sci Transl Med. 2024;16:eadg1323. https://doi.org/10.1126/scitranslmed.adg1323

23. Hansen LMB, Dam VS, Guldbrandsen HØ, Staehr C, Pedersen TM, Kalucka JM, et al. Spatial Transcriptomics and Proteomics Profiling After Ischemic Stroke Reperfusion: Insights Into Vascular Alterations. Stroke. 2025;56:1036–1047. https://doi.org/10.1161/strokeaha.124.048085

24. Li H, Liu P, Zhang B, Yuan Z, Guo M, Zou X, et al. Acute ischemia induces spatially and transcriptionally distinct microglial subclusters. Genome Med. 2023;15:109. https://doi.org/10.1186/s13073-023-01257-5

25. Zucha D, Abaffy P, Kirdajova D, Jirak D, Kubista M, Anderova M, et al. Spatiotemporal transcriptomic map of glial cell response in a mouse model of acute brain ischemia. Proc Natl Acad Sci U S A. 2024;121:e2404203121. https://doi.org/10.1073/pnas.2404203121

26. Xia X, Lemieux ME, Li W, Carroll JS, Brown M, Liu XS, et al. Integrative analysis of HIF binding and transactivation reveals its role in maintaining histone methylation homeostasis. Proc Natl Acad Sci U S A. 2009;106:4260–4265. https://doi.org/10.1073/pnas.0810067106

27. Benita Y, Kikuchi H, Smith AD, Zhang MQ, Chung DC, Xavier RJ. An integrative genomics approach identifies hypoxia-inducible factor-1 (HIF-1)-target genes that form the core response to hypoxia. Nucleic Acids Res. 2009;37:4587–4602. https://doi.org/10.1093/nar/gkp425

28. Zimmerman KD, Espeland MA, Langefeld CD. A practical solution to pseudoreplication bias in single-cell studies. Nat Commun. 2021;12:738. https://doi.org/10.1038/s41467-021-21038-1

29. Cheng J, Teply BA, Sherifi I, Sung J, Luther G, Gu FX, et al. Formulation of functionalized PLGA-PEG nanoparticles for in vivo targeted drug delivery. Biomaterials. 2007;28:869–876. https://doi.org/10.1016/j.biomaterials.2006.09.047

30. Lv LZ, Tong CQ, Lv Q, Tang XJ, Li LM, Fang QX, et al. Enhanced absorption of hydroxysafflor yellow A using a self-double-emulsifying drug delivery system: in vitro and in vivo studies. Int J Nanomedicine. 2012;7:4099–4107. https://doi.org/10.2147/ijn.s33398

31. Hu X, Zhang J, Deng L, Hu H, Hu J, Zheng G. Galactose-Modified PH-Sensitive Niosomes for Controlled Release and Hepatocellular Carcinoma Target Delivery of Tanshinone IIA. AAPS PharmSciTech. 2021;22:96. https://doi.org/10.1208/s12249-021-01973-4

32. Jaakkola P, Mole DR, Tian YM, Wilson MI, Gielbert J, Gaskell SJ, et al. Targeting of HIF-alpha to the von Hippel-Lindau ubiquitylation complex by O2-regulated prolyl hydroxylation. Science. 2001;292:468–472. https://doi.org/10.1126/science.1059796

Supplementary Files

This is a list of supplementary files associated with this preprint. Click to download.

- SupportingInformation.docx
- GraphicalAbstract.pptx